Journal of Energy Storage 94 (2024) 112326

Contents lists available at ScienceDirect

Journal of Energy Storage

journal homepage: www.elsevier.com/locate/est

Research Papers

Critical comparison of equivalent circuit and physics-based models for lithium-ion batteries: A graphite/lithium-iron-phosphate case study

Marco Lagnoni [a,*], Claudio Scarpelli [b,*], Giovanni Lutzemberger [b], Antonio Bertei [a]

[a] Department of Civil and Industrial Engineering, University of Pisa, Pisa, Italy
[b] Department of Energy, Systems, Territory and Constructions Engineering, University of Pisa, Pisa, Italy

ARTICLE INFO

Keywords:
Thermo-electrochemical Li-ion battery modelling
Equivalent circuit model
Physicsbased model
Models accuracy assessment

ABSTRACT

Accurate modelling of Li-ion batteries is essential for optimising performance and safety across a range of applications, from electric vehicles (EVs) to grid storage. This paper critically evaluates two prevalent battery modelling methodologies: Equivalent Circuit Model (ECM) and Physics-Based Model (PBM), using a 60 Ah prismatic graphite/lithium-iron-phosphate battery as a case study. The focus of this work is on developing, parameterising, and cross-validating these approaches through a comprehensive set of electrical tests at different ambient temperatures under constant and variable current densities, including the Worldwide Harmonised Light Vehicles Test Cycle (WLTC) protocol. This evaluation not only assesses the accuracy and reliability of the ECM and PBM but also underscores their strengths and limitations. The ECM shows advantages in computational speed, ease of calibration, and accuracy within its calibration range and for variable current profiles. However, its accuracy diminishes at higher currents, especially for prolonged current pulses, and beyond the calibration range, as evidenced in charging scenarios beyond 1C. Conversely, the PBM maintains accuracy beyond the calibration dataset but necessitates estimation of many physical parameters, a laborious calibration process, and extended computational times for variable current scenarios. Within the range of conditions investigated (from C/3 to 2C between 10 °C and 40 °C), the average errors in voltage prediction are 51.5 mV for ECM and 19.3 mV for PBM, while 0.9 °C for ECM and 0.4 °C for PBM in temperature prediction. In summary, while the ECM is suited for reproducing constant discharges or WLTC-like profiles with brief and low-intensity charge pulses, the PBM strength lies in its predictiveness for high-rate operations, making them complementary tools for simulating realistic EV load operations and for optimising fast-charging protocols, respectively. These insights contribute to the ongoing advancement of battery technology, focusing on realistic and applicable model development and parameterisation.

1. Introduction

Li-ion batteries, integral to a myriad of applications from electric vehicles (EVs) to renewable energy storage, are a cornerstone of contemporary energy solutions [1,2]. Their complex behaviour and performance characteristics necessitate precise modelling for optimisation and understanding [3–6]. In the field of Li-ion battery modelling, two predominant methodologies have emerged: equivalent circuit models (ECMs) and physics-based models (PBMs) [7,8]. Each of these approaches has been extensively applied in the literature, reflecting a diverse array of modelling objectives and scenarios [9–16].

ECMs conceptualise the battery as an electrical network comprising resistors, capacitors, and voltage sources [13,17,18]. This analogy into an electrical framework simplifies the battery intricate internal processes, a feature that has been widely acclaimed in the literature for its computational efficiency and ease of integration into simulation tools and battery management systems [9,19,20]. The adaptability of ECMs across different battery types, sizes, and geometries, with minimal calibration data, is particularly noted in various studies, enhancing their appeal for real-time applications and general condition estimations [17,19,21–23]. However, limitations of ECMs are evident in their superficial handling of the battery internal physical and chemical dynamics, such as ion diffusion and electrochemical reactions [8]. This lack of depth in representing internal processes often results in compromised predictive accuracy under extreme conditions or in the development of novel battery chemistries [24].

---

* Corresponding authors.
E-mail addresses: marco.lagnoni@unipi.it (M. Lagnoni), claudio.scarpelli@unipi.it (C. Scarpelli).

https://doi.org/10.1016/j.est.2024.112326
Received 31 January 2024; Received in revised form 7 May 2024; Accepted 26 May 2024
2352-152X/© 2024 The Authors. Published by Elsevier Ltd. This is an open access article under the CC BY license (http://creativecommons.org/licenses/by/4.0/).

On the other hand, PBMs are rooted in the fundamental physical and chemical underpinnings of battery operation, including the principles of mass and charge conservation, diffusion, and reaction kinetics [25–28]. The PBMs are promoted for their ability to provide detailed insights into internal processes like concentration and temperature gradients, which are crucial for probing new battery chemistries and predicting behaviour under a variety of operational scenarios [29–33]. Their comprehensive nature makes PBMs invaluable tools for in-depth analysis and exploration, as they can capture complex interactions within the battery that ECMs might overlook. However, the intricate nature of PBMs comes with its own set of challenges, as noted in various studies [3,7,34]. The high computational demands of these models and the necessity for extensive experimental data for calibration and validation purposes are significant drawbacks [35]. These requirements limit PBMs immediate applicability in real-time systems or contexts requiring rapid and efficient modelling [36].

To bridge the gap between ECMs and PBMs, a hybrid approach that combines the strengths of both methodologies has been explored in recent research, that is the development of hybrid physics-based equivalent circuit models [37–39]. These advanced equivalent circuit models incorporate physical and chemical principles, offering a more robust representation of the battery internal processes, while maintaining the computational efficiency of traditional ECMs [40,41]. This combination allows for efficient, real-time applicability while maintaining a deeper understanding of key phenomena such as diffusion, kinetic reactions, and concentration gradients [40,42–44]. Physics-based ECMs offer a balanced solution by capturing battery behaviour across a range of operating conditions, including high-rate charging and discharging cycles [42]. Nevertheless, precise parameter identification and the complexity of modelling intricate battery dynamics [3,45–47] remain challenges which still require PBMs to provide accurate predictions.

To explore the full range of these possible modelling approaches, this work focusses on ECM and PBM critical comparison. While existing literature includes works that compare the capabilities of both ECM and PBM methods, even when applied to real case studies [48,49], there is still limited evidence of studies applying these two methods to the same battery and independently assessing their results using a shared set of experimental tests. Therefore, this research aims to critically compare the ECM and PBM performance on the same experimental dataset providing a balanced perspective of both approaches. A validated comparative framework applied to a commercial graphite/Li-iron-phosphate (LFP) battery evaluates model effectiveness across various temperature and operational scenarios. The examination includes their respective limitations, identifying their applicability ranges and potential areas for improvement. This analysis extends to the application of these models to the Worldwide Harmonised Light Vehicles Test Cycle (WLTC) protocol [50], exploring the challenges and opportunities of employing ECMs and PBMs in vehicular technology settings [51,52]. While this study uses the WLTC protocol to evaluate Li-ion batteries, primarily used in electric vehicles, the growing use of these LFP batteries in stationary storage systems is also acknowledged; in any case, the findings of the study will remain robust across various application settings, including those with less dynamic operation rates [53,54]. Overall, this research offers a comprehensive examination of the dominant modelling methodologies in Li-ion battery research, with the goal of advancing both theoretical understanding and practical application in this rapidly evolving field.

The structure of the paper is as follows. Section 2.1 introduces the cell under investigation, detailing its internal characterisation and the electrical procedures used to generate the dataset for model testing. Subsequently, Sections 2.2 and 2.3 delineate the mathematical frameworks and key parameters of the ECM and PBM, respectively. Section 3.1 focuses on the calibration procedures for these models, while in Section 3.2 the calibrated models are cross-validated in a wider spectrum of operational conditions beyond their calibration dataset, critically comparing model predictions in terms of average and maximum deviations from experimental data. Finally, the application of the models to a WLTC scenario examines the practical efficacy and constraints of ECM and PBM in dynamic EV applications, leading to the final conclusions in Section 4.

2. Methods

2.1. *Investigated cell and electrical characterisation methods*

In this research, a 60 Ah Li-ion battery with a prismatic geometry (Fig. S1) is analysed to parametrise and validate the ECM and the PBM. The battery specifications, based on data sheets and prior material characterisations [51,52,55], are detailed in Table 1.

Understanding the definition of C-rate is crucial for this study. All C-rates mentioned are given with respect to the nominal capacity (C_{nom}), i.e., 60 Ah, with 1C equating to 60 A. Thus, the current is defined as the product of the C-rate n (with units of h^{-1}) times the nominal capacity of the cell, resulting in a current corresponding to nC_{nom}.

The battery testing setup included a climatic chamber (Binder KB 115), where the battery was placed, connected to a Digatron® battery cycler (6 V, 250 A) (Fig. S1). This cycler executed specific load profiles at varying ambient temperatures, with details in Table S1, and monitored the battery voltage and current. To measure cell surface temperature, nine K-type temperature probes were affixed to its lateral surfaces, with an additional probe for room air temperature placed in the chamber upper section. The climatic chamber ambient conditions were controlled to match test requirements, with tests conducted in free air, supported by low forced convection from an air fan.

Capacity tests were performed at C/3 (20 A) to determine the accessible capacity using a constant current constant voltage (CCCV) (CC phase cut-off at V = 3.65 V, CV phase cut-off current C/20 = 3 A) charge and a C/3 discharge protocol resulting in 62 Ah. Multiple step test (MST) protocols, also known as galvanostatic intermitted titration technique tests (GITT), were conducted to capture the battery electrical behaviour in response to a series of discharging current steps. This test involved multiple 1C (60 A) current pulses of 6 min duration (6 Ah), interspersed with 1-h rest phases, systematically reducing the battery state of charge (SOC) by 10 % after each step, starting from a fully charged state (Fig. S2). Following the MST, charge (CHA) and discharge (DCH) tests were performed to evaluate the battery behaviour under standard profiles recommended by the manufacturer. The constant current (CC) phase of charge tests was conducted at two rates, C/2 (30

Table 1
Characteristic data of the cell.

Battery specifics	Battery internal characterisation
Chemistry and type: Graphite/LFP - Prismatic	No. of active layers N_{cell}: 176
Dimensions: 130 × 186 × 36 mm	Electrode cross-section area A_{act}: 0.0193 m^2
Weight: 1.685 kg	Copper current collector thickness L_{CC_N}: 7.9 μm
Voltage range: 2.8–3.65 V	Aluminium current collector thickness L_{CC_P}: 11.6 μm
Nominal voltage: 3.2 V	Negative electrode thickness L_N: 72.5 μm
Max discharge current: 180 A	Positive electrode thickness L_P: 76.1 μm
Max charge current: 90 A	Separator thickness L_S: 25 μm
Charging method: CC-CV (CC until 3.65 V, CV cut-off current = C/20)	Graphite particle radius r_N: 10.0 μm
Operating temperature: −20 to 50 °C (discharging @ < 0.3C), 0 to 50 °C (charging @ < 0.3C)	LFP particle radius r_P: 36.5 nm
Gravimetric energy: 113 Wh kg^{-1}	Active volume V_{act}: 6.577 10^{-4} m^3
Volumetric energy: 220 Wh L^{-1}	External cooled surface A_{ext}: 0.0520 m^2

A) and 1C (60 A), beginning with the battery fully discharged to ensure a zero SOC (Fig. S3). The discharging tests involved initially fully charging the battery using a CCCV protocol (as per capacity tests), and then a single CC phase discharging until the voltage reached 2.8 V, at C/3 (20 A), C/2 (30 A), 1C (60 A), and 2C (120 A). All tests were repeated at three different ambient temperatures: 10, 25, and 40 °C. The Worldwide Harmonised Light Vehicles Test Cycle (WLTC) protocol was conducted to simulate a dynamic vehicular scenario, applying a current profile that mirrors an electric vehicle battery performance. The current profile was adjusted to stay within the battery operational limits, with a maximum discharge current of 115 A. The test began with the battery at 90 % SOC and was repeated until the battery reached full discharge (2.8 V minimum voltage threshold), conducted at 10 and 20 °C (Fig. S4).

MSTs calibrated ECM parameters, while C/2 charge tests calibrated PBM parameters, ensuring a comparable number of calibration datasets for the models (namely, one per temperature). After calibration, all tests were simulated using both models for cross-validation, focusing on differences in voltage and temperature behaviour predictions. Lastly, the WLTC tests evaluated the potential and limits of both models, particularly for on-line monitoring applications.

In short, these tests provided a comprehensive analysis of the battery performance under different operational conditions within manufacturer-specified limits and safety guidelines. The chosen ranges aimed to avoid significant degradation mechanisms not included in the current iteration of ECMs and PBMs used in this study. Despite this, the approaches presented here can be generalised to broader conditions if degradation phenomena are mathematically described and included in the modelling frameworks. The results are fundamental for calibrating and validating the ECM and PBM, as discussed in Section 3. Table 2 outlines the details of the electrical tests, including test reference number, types, and operational temperatures in the climatic chamber.

2.2. Equivalent circuit model

2.2.1. Mathematical framework

To predict the electrical and thermal behaviour of the battery, two coupled equivalent circuit models are required: an Electrical-ECM and a Thermal-ECM. These two models can be both calibrated and verified experimentally using measurements of parameters like cell output voltage, current, and temperature that can be easily obtained without causing any harm to the cell itself, considering the latter as a “black box”.

The Electrical-ECMs for Li-ion batteries have been extensively documented in various research works [8,9]. A common approach in these models is the utilisation of an *n*-RC network, where *n* can be 0, 1, 2, or more. This network consists of a series of resistor-capacitor (RC) parallel circuits, which are instrumental in simulating the dynamic responses of the battery [52,55]. Among the different ECMs, the most prevalent ones fall under the *n*-RC category, which includes the 0-RC model, the 1-RC model, and the 2-RC model. While incorporating more RC blocks into the ECM can enhance the accuracy in depicting the battery behaviour characteristics, it simultaneously escalates the complexity of the mathematical framework. This increase in complexity can pose challenges in model parameter identification and *SOC* estimation, which are critical functions of the Battery Management System (BMS). Thus, a 2-RC model has been selected for this study as commonly found in the literature [56,57].

Table 2
Electrical test procedures and ambient temperature conditions.

Test reference number	Type of test	Ambient temperature (°C)
1	Multiple step test (MST)	
2	Charge CC-CV C/2	
3	Charge CC-CV 1C	
4	Discharge CC C/3	10, 25, 40
5	Discharge CC C/2	
6	Discharge CC 1C	
7	Discharge CC 2C	
8	WLTC	10, 20

A schematic of the Electric-ECM is reported in Fig. 1a, the latter is represented by a one-port electric circuit comprised of an ideal voltage generator V_{OC} in series to a longitudinal pure resistance R_0 and two longitudinal resistance-capacitor parallel blocks (R_1, C_1 and R_2, C_2). V_{OC} replicates the battery open circuit voltage (i.e., the battery measurable voltage when no current is applied), R_0 simulates the battery ohmic behaviour, i.e., the immediate proportional voltage change as current is applied, while R_1, C_1 and R_2, C_2 allow the model to capture the battery dynamics occurring at different timescales in the order of minutes (charge-transfer processes) and tens of minutes (diffusion processes), respectively. As a remark, it is important to consider that the electrical components vary in function of the physical conditions of the battery itself. Indeed, each Electric-ECM element is potentially dependent on several variables, such as the battery temperature (T), state of charge (SOC), aging and healthy conditions (commonly named as state of health, SOH). Here, the Electrical-ECM parameters are assumed to be 2-dimension variables only, as function of T and SOC, while the dependence on SOH is neglected.

The structure of the Thermal-ECM used in this work is represented by a lumped temperature model [55,58], whose schematics is reported in Fig. 1b. The battery thermal dynamics is simulated via a single temperature value T and a unique battery thermal mass Mc_p, where M is the battery mass and c_p its equivalent specific heat. The heat generated by the battery is modelled with the ideal power generator q_{gen}, while q_{ex} represents the heat exchanged with the surrounding environment T_{amb} through the convective resistance R_{conv}.

2.2.2. Parametrisation

The Electrical-ECM and Thermal-ECM, reported in Fig. 1, are calibrated using MST results obtained at 10, 25 and 40 °C ambient temperature, where each pulse plus relax-phase is analysed to parametrise their components.

A typical discharging step of the MST, along with the corresponding battery SOC and voltage profiles, begins from a stable electrical condition. The current step, with intensity I_{app} (60 A) and duration Δt (6 min), results in a change in SOC (10 %), calculated using ampere-hour counting based on the battery nominal capacity ($C_{nom} = 60$ Ah). The battery voltage is monitored until system relaxation, i.e., when the voltage is flat, providing the open circuit voltage (OCV) at different SOC values, which correspond to V_{OC} in Fig. 1a.

Notably, electrical parameters derived from a single MST are temperature-dependent. To ensure accuracy, the applied current I_{app} is kept relatively small to avoid significant temperature variations in the battery (Fig. S2). Thus, each electrical parameter is calibrated as a function of SOC and $T_{amb} = 10, 25, 40$ °C. The open circuit voltage V_{OC} of the battery is evaluated as the collection of datapoints obtained after complete relaxation at various SOC levels for each value of T_{amb}. The resulting function is $V_{OC} = V_{OC,ref} + EHC_{cell}\left(T_{cell} - T_{ref}\right)$, where $T_{ref} = 25^{\circ}C$ and $EHC_{cell} = \frac{\partial V_{oc}}{\partial T}$ is the entropic heat coefficient obtained as linear interpolation between V_{OC} data centered at 25 °C.

The longitudinal pure resistance R_0 is calculated from the instantaneous voltage drop (ΔV_a) post-current step (Eq. (1)). The remaining

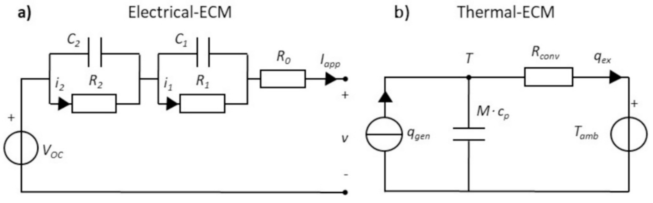

Fig. 1. Schematics of the Electrical-ECM (a) and the Thermal-ECM (b).

parameters, namely the two parallel RC blocks (R_1, C_1, R_2, C_2), are extracted from the analysis of the voltage evolution during the relax-phase. In such a phase, the battery voltage v is modelled by the Electrical-ECM through the sum of the transient decays of the RC blocks (Eq. (2)), each with a specific characteristic time τ_n with $n = 1{,}2$ (Eqs. (3), (4)), until the energy of every capacitance is dissipated in its respective resistor. In Eq. (2) i_1 and i_2 are the unknown values of the current flowing in R_1 and R_2 respectively, at time equal to t. Notably, in the impossibility of knowing any information of how the total dynamic voltage drop (ΔV_d) is divided among the two RC blocks (Eq. (5)), the optimisation routine implemented in the Design Library of Dymola software [59] was used, which is also the software used for creating and simulating both Electrical and Thermal ECMs. This routine involves setting initial guess values for these parameters, initialising the model with the starting SOC and T_{ref}, and inputting the experimental current step profile. The optimisation iteratively adjusts R_1, C_1, R_2, C_2 to minimise the Root Mean Square Error (RMSE) between the simulated and experimental voltage curves.

This procedure is repeated for every step involved in the MST and every ambient temperature. After that, the complete set of Electrical-ECM parameters is provided, with all the circuital elements defined as a function of discrete SOC and temperature values. In this work, the model is parameterised with 10 values of SOC equally distributed from 100 % to 0 %, and three values of ambient temperature that are 10, 25 and 40 °C as reported in Fig. A1 (numerical parametrisation of ECM electrical parameters is provided in the Supplementary information Tables S2 and S3).

Regarding the parametrisation of the Thermal-ECM, the equivalent specific heat c_p for the battery under analysis was already estimated experimentally in a previous study of this group [51], so its measurement procedure will not be reported here. Also, it is important to underline that the predicted battery temperature T is meant to represent an indication of the average surface cell temperature. Therefore, for calibration purposes of this paper, T will be compared with the average value of the measurements of the 9 thermal probes places on the surface of the battery itself. In Fig. 1b, the convective resistance R_{conv} is defined by Eq. (6), where A_{ext} is the battery outer surface and h is the convective heat coefficient [51,52], both known from the battery geometrical properties and the heat exchange capacity of the climatic chamber where the battery is placed in. The generated heat q_{gen} is composed by two sources, as in Eq. (7). The first one is the irreversible heat q_{irr} (Eq. (8)) which corresponds to the total Joule losses in the Electrical-ECM, while the second source is the reversible heat q_{rev} (Eq. (9)), also named as “entropic heat”, which can be addressed to cell internal entropic changes effects, as in [52]. Regarding the modelling of irreversible heat, it is necessary to clarify the following. For the ECM adopted in this work, the contribution q_{irr} is modelled as the heat produced by the Joule effect from the resistors of the equivalent circuit of Fig. 1a, as in Eq. (8), according to [52,60]. In addition to this modelling approach, in the literature the q_{irr} term for ECMs is often modelled as a simple product $(V_{OC} - V)I_{app}$, where V_{OC} is the open-circuit voltage of the battery and I_{app} is the current at the output terminals [61–63]. Comparing this latter expression with Eq. (8), the two are equivalent only at electrical steady-state, i.e., when the current in the capacitors of Fig. 1a is equal to zero, and so $i_1 = i_2 = I_{app}$. Therefore, the two models differ only under transient conditions. A key physical difference between the two approaches is that the model $q_{irr} = (V_{OC} - V)I_{app}$ suggests there are no irreversible losses if the current at the battery terminals is zero, and thus in all cases of voltage relaxation. This is believed to be incorrect as, even during relaxation, the battery experiences transient internal charge transfer phenomena, which cannot be assumed to result in zero losses. However, from a qualitative comparison regarding the expected difference in cell temperature using either approach, it can be reasonably stated that the approach in Eq. (8) estimates a higher average generated heat compared to the other, as it accounts for the heat dissipated during dynamic relaxation phases as well. From this perspective, it can be considered a more conservative method for estimating the maximum temperatures reached. Additionally, while q_{irr} contribution is always positive, the sign of q_{rev} depends on the sign of I_{app} (if the cell is charging, < 0, or discharging, > 0) as well as the sign of EHC_{cell}, which varies with the SOC (Table S3). Therefore, q_{rev} can either act as an additional cell heating effect ($q_{rev} > 0$) or as a cooling effect ($q_{rev} < 0$). Further information about all the parameters of the battery Thermal-ECM adopted in this work are reported in Appendix A as well as in the Supplementary information. Key equations discussed in this section are reported in Table 3.

2.3. Physics-based model

2.3.1. Mathematical framework

In this study, the selected physics-based model for battery simulation is the Pseudo-2-Dimensional (P2D) framework, firstly introduced by Doyle, Fuller, and Newman [27,64]. This model, based on porous electrode theory, offers a macroscale homogenous description of charge and mass conservation in both the solid phase (s), representing the electrode active material, and the liquid phase (ey), which relates to the electrolyte. The model treats each unit cell component as a continuum, incorporating microstructural information (e.g., volume fraction ε_i, tortuosity factor τ_i, with $i =$ phase) and particle properties (e.g., radius r, specific surface area A_{am}) through effective transport and kinetic parameters. As reported in Fig. 2, a battery unit cell comprises current collectors (CC), negative (N) and positive (P) electrodes, and a separator (S). The unit cell through-thickness coordinate (x) is treated as a 1D domain, which is coupled with Li transport within the radial coordinate (y) of the active material, introducing an additional pseudo-dimension [65,66].

In the electrode thickness direction, the model solves the conservation of mass (Eqs. (10a)–(10b)) and charge (Eqs. (11a)–(11b)) for Li ions. This involves solving for their concentration and reduced electrochemical potential in the electrolyte, c and $\widetilde{\mu}^*_+$, respectively [25,67]. As in Eqs. (10b) and (11b), J_{conc} and J_2 represent the Fick-like diffusional flux of Li-ions and the total ionic current density in the electrolyte phase, respectively. The coupling of the 1D through-thickness domain with the pseudo 1D radial direction in the solid phase is achieved through the charge transfer reaction. The latter is depicted by the current density at the particle interface J_{ct} (Eqs. (12a)–(12c)), here modelled using a Butler-Volmer kinetics. Within the electrode, the potential in the electron-conductive phase (el), $\widetilde{\mu}^*_{\mathrm{e}}$ (i.e., the reduced electrochemical potential of electrons [25]), is determined using Ohm law (Eqs. (13a)–(13b)). Then, the Li mass conservation equation in the electrode active material solves for the concentration of intercalated Li, c_s (Eqs. (14a)–(14d)).

Additional clarification is needed regarding the modelling of Li transport within the active materials used in this study. The definition of Li flux, N_s, along the particle radius is different between graphite and LFP materials. While both materials are known to undergo phase-separation during lithiation [31,46,68–71], this study solves phase-

Table 3

Mathematical framework of the Electrical-ECM and Thermal-ECM.

$$R_0 = \frac{\Delta V_a}{\Delta I} \tag{1}$$

$$v(t) = V_{OC} - R_1 i_1(t) e^{-\frac{t}{\tau_1}} - R_2 i_2(t) e^{-\frac{t}{\tau_2}} \tag{2}$$

$$\tau_1 = R_1 C_1 \tag{3}$$

$$\tau_2 = R_2 C_2 \tag{4}$$

$$\Delta V_d = R_1\left(SOC_n, T_{ref}\right) i_1(t) + R_2\left(SOC_n, T_{ref}\right) i_2(t) \tag{5}$$

$$R_{conv} = \frac{1}{h A_{ext}} \tag{6}$$

$$q_{gen} = q_{irr} + q_{rev} \tag{7}$$

$$q_{irr} = R_0 i^2 + R_1 i_1^2 + R_2 i_2^2 \tag{8}$$

$$q_{rev} = -\, i_{cell} T_{cell} EHC_{cell} \tag{9}$$

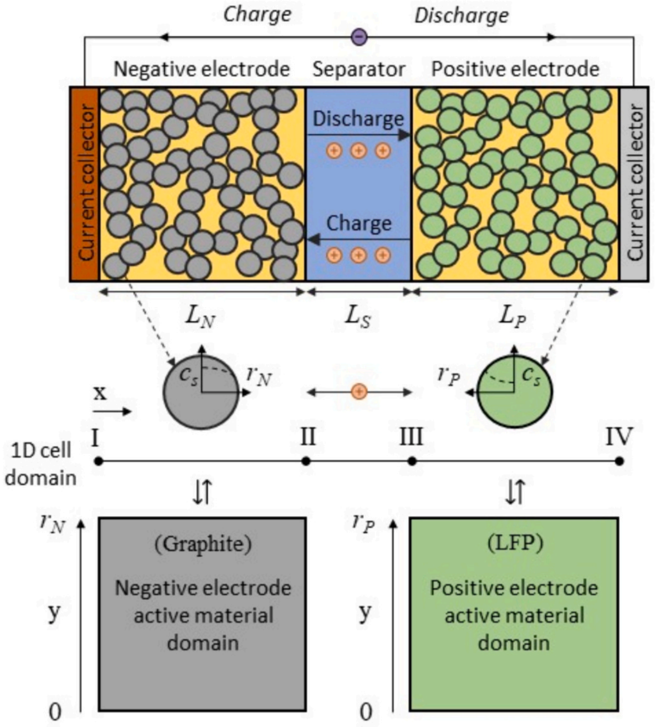

Fig. 2. Schematics of the P2D mathematical domain for the simulations of the cell. The through-thickness 1D direction x reports the thickness of the graphite/LFP cell, which is coupled to the additional pseudo 1D radial direction y for Li solid-state diffusion along the radius of the active material particles.

separation via the phase-field approach exclusively for the graphite electrode (Eq. (14b)) [72,73]. In this approach, Li flux is driven by the gradient of chemical potential μ, which is linked to the equilibrium potential of graphite ($U_{eq,N}$) and accounts for the interface thickness (a) between stable phases, which have been fully characterised in previous studies by the authors [3,30]. On the other hand, Li diffusion within LFP particles is described according to the traditional Fick's law, where $D_{s,P}$ is the chemical diffusivity (Eq. (14c)). This simplified approach does not capture the full intricacies of phase separation in LFP, nor does it account for LFP hysteresis [74,75], but it reduces computational time and is sufficient for the scope of the PBM, which aims to predict cell-level variables such as cell voltage and temperature. Given the small diffusion timescale in nanometric LFP particles [76,77], this approach is appropriate for the analysis in this study.

Aligning with the Thermal-ECM presented in Section 2.2, temperature change in the battery is considered by enforcing a lumped energy conservation equation, as the temperature distribution within the unit cell can be approximated as uniform [51,52,78]. Following this approach, the cell thermal evolution is simulated via a single temperature value T which depicts the average temperature of the battery over time, and a unique cell thermal mass (Mc_p) using Eqs. (15a)–(15b). In Eq. (15a), the quantity $hA_{ext}(T - T_{amb})$ represents the heat removed by convection, while $\dot{q}_V$ is the total volumetric heat generated in the unit cell. The latter is given by the summation of the volumetric heat generated in the negative and positive electrodes, and in the separator, as in Eq. (15b). Notably, the current collectors volumetric heat generation has been neglected in this study as its contribution, that is purely ohmic, is small compared to that of the other unit cell components given the very high electrical conductivity of the current collector materials [78,79]. Each volumetric contribution from the unit cell components is obtained by integral averaging the specific heat per unit of cross-sectional area generated in each domain over the corresponding thickness (Eq. (16a)). Following the well-established framework introduced by Bernardi et al. [28], three major heat contributions define the heat generated in the unit cell: i. the reversible heat $\dot{Q}_{rev}$ (Eq. (16b)) associated to the entropic change of charge-transfer phenomena, ii. the irreversible heat $\dot{Q}_{rxn}$ (Eq. (16c)) associated to the activation overpotential of electrochemical reactions, and iii. the ohmic heat $\dot{Q}_{ohm}$ (Eq. (16d)) associated to the Joule dissipations occurring in electrolyte and solid phases. By solving the thermal model, the temperature evolution of the battery can be coupled to the electrochemical model to update equilibrium, transport, and kinetics parameters over time during the simulation (Eqs. (17a)–(17d)).

Since the equations of the P2D thermo-electrochemical model are consolidated in the literature, the reader is referred to specific papers and textbooks for their derivation [26–28,64,65,80], only a brief description of the model key equations (Table 4) and quantities is reported here; detailed boundary conditions for the electrochemical model are outlined in Appendix B, and corresponding nomenclature is provided at the end of the manuscript.

Table 4
Governing equations and key quantities of the P2D electrochemical model and lumped thermal model.

Electrochemical model framework

Electrolyte phase $i = N, S, P$

$$\varepsilon_{ey,i} F \frac{\partial c}{\partial t} + \frac{\partial}{\partial x}(J_{conc}) = (1 - t_+) J^V_{ct,i} \tag{10a}$$

$$J_{conc} = -\frac{\varepsilon_{ey,i}}{\tau_{ey,i}} F \widetilde{D} \frac{\partial c}{\partial x} \tag{10b}$$

$$\frac{\partial}{\partial x}(J_2) = J^V_{ct,i} \tag{11a}$$

$$J_2 = -\frac{\varepsilon_{ey,i}}{\tau_{ey,i}} \sigma \frac{\partial \widetilde{\mu}^*_+}{\partial x} + \frac{\varepsilon_{ey,i}}{\tau_{ey,i}} \sigma \frac{2RT}{F} (1 - t_+) \gamma_\pm \frac{\partial lnc}{\partial x} \tag{11b}$$

Interfacial equations $i = N, P$

$$J^V_{ct,i} = J_{ct,i} A_{am,i} \tag{12a}$$

$$J_{ct,i} = k_{ct,i} c^\alpha \left(c^{max}_{s,i} - c_{s,i}\right)^\alpha c_{s,i}{}^{(1-\alpha)} \left[exp\left(\frac{\alpha F}{RT} \eta_{ct,i}\right) - exp\left(-\frac{(1-\alpha)F}{RT} \eta_{ct,i}\right)\right] \tag{12b}$$

$$\eta_{ct,i} = \widetilde{\mu}^*_{e,i} - \widetilde{\mu}^*_+ - U_{eq,i} \tag{12c}$$

Electro-conductive phase $i = N, P$

$$\frac{\partial}{\partial x}(J_{1,i}) = -J^V_{ct,i} \tag{13a}$$

$$J_{1,i} = -\sigma_{e,eff,i} \frac{\partial \widetilde{\mu}^*_{e,i}}{\partial x} \tag{13b}$$

Active material phase $i = N, P$

$$\frac{\partial c_{s,i}}{\partial t} + \frac{\partial}{\partial y}(N_{s,i}) = -\frac{2}{y} N_{s,i} \tag{14a}$$

$$N_{s,N} = -\frac{1}{RT} \overline{D}_{s,N} c_{s,N} \frac{\partial \mu}{\partial y} \text{ valid for N} \tag{14b}$$

$$N_{s,P} = -D_{s,P} \frac{\partial c_{s,P}}{\partial y} \text{ valid for } P \tag{14c}$$

$$\mu = \mu_{eq} - RTa^2 \frac{\partial^2 \widetilde{c}_{s,N}}{\partial y^2} \text{ valid for N} \tag{14d}$$

Lumped thermal model framework

$$Mc_p \frac{dT}{dt} = \dot{q}_V V_{act} - hA_{ext}(T - T_{amb}) \tag{15a}$$

$$\dot{q}_V = \left(\dot{q}_N + \dot{q}_S + \dot{q}_P\right) \tag{15b}$$

$$\dot{q}_i = \int \left(\dot{Q}_{rev,i} + \dot{Q}_{rxn,i} + \dot{Q}_{ohm,i}\right) \frac{dx}{L_{tot}} \; i = N, S, P \text{ and } L_{tot} = L_N + L_S + L_P \tag{16a}$$

$$\dot{Q}_{rev,i} = J^V_{ct,i} \, T \, EHC_i \; i = N, P \tag{16b}$$

$$\dot{Q}_{rxn,i} = J^V_{ct,i} \eta_{ct,i} \; i = N, P \tag{16c}$$

$$\dot{Q}_{ohm,i} = \frac{\varepsilon_{el,i}}{\tau_{el,i}} \sigma_{el,i} \left(\frac{\partial \widetilde{\mu}^*_{e,i}}{\partial x}\right)^2 + \frac{\varepsilon_{ey,i}}{\tau_{ey,i}} \sigma \left(\frac{\partial \widetilde{\mu}^*_+}{\partial x}\right)^2 - \frac{\varepsilon_{ey,i}}{\tau_{ey,i}} \frac{2RT\sigma}{F} (1 - t_+) \gamma_\pm \frac{\partial lnc}{\partial x} \frac{\partial \widetilde{\mu}^*_+}{\partial x} \; i = N, S, P \tag{16d}$$

Transport, kinetics, and equilibrium parameters

$$U_{eq,N} = E^\circ - \frac{\mu}{F} + (T - T_{ref}) EHC_N \tag{17a}$$

$$U_{eq,P} = U_{eq,ref,P} + (T - T_{ref}) EHC_P \tag{17b}$$

$$D_{s,i} = D^\circ_{s,i} exp\left(-\frac{E_{D_{s,i}}}{R}\left(\frac{1}{T} - \frac{1}{T_{ref}}\right)\right) \; i = N, P \tag{17c}$$

$$k_{ct,i} = k^\circ_{ct,i} exp\left(-\frac{E_{k_{ct,i}}}{R}\left(\frac{1}{T} - \frac{1}{T_{ref}}\right)\right) \; i = N, P \tag{17d}$$

2.3.2. Parametrisation

The physics-based model is a powerful tool which can provide accurate predictions on battery dynamics; however, it requires an extensive and consistent parametrisation. Building on the specifications introduced in Section 2.1, the parametrisation of the thermal-electrochemical model for the 60 Ah graphite/LFP battery, comprising 176 unit cells, follows a systematic approach. The parametrisation process starts from the rated capacity ($C_{rated} = 62$ Ah), derived from capacity tests, to calculate the rated capacity per unit cross-sectional area for a single unit cell ($C_{cell} = \frac{C_{rated}}{N_{cell}A_{act}}$), resulting in 18.21 Ah m^{-2}. Then, a series of educated guesses, calculations, and fitting of the calibration dataset (i.e., C/2 charging at three different ambient temperatures) are required to provide a complete parametrisation, as described in the following.

For the graphite electrode, geometrical (e.g., electrode thickness L, particle average radius r), electrochemical (e.g., maximum Li concentration c_s^{max}), equilibrium (U_{eq}), and transport parameters (e.g., diffusion coefficient $\overline{D}_s^{\circ}$) are selected based on a comprehensive literature survey along with prior studies and measurements [3,30,51,69,78,81,82]. The LFP cathode requires similar parameters, which have been evaluated starting from the identification of plausible ranges from the literature. Such an analysis was carried out using Liiondb, a general database for battery materials properties and parameters, to locate papers specifically focusing on LFP, along with specific papers not available in the database [10,29,83–92].

For both electrodes, active material volume fractions and operative states of lithiation are evaluated in this work to match the area-specific rated capacity and equilibrium cell potentials at full charge/discharge. The microstructural parameters, as the volume fractions and tortuosity factors of different phases in the unit cell composites, were not previously measured for this specific cell. For graphite, the volume fraction of the filler phase ε_{fill} is assumed to be 0.057, while for LFP it is set to 0.1, which includes the electron-conductive phase ε_{el}, in agreement with literature data [78,83,91,93]. The volume fractions of graphite and LFP active materials are derived from the fitting of C/2 charge tests and the operative state of lithiation windows $\widetilde{c}_s^{min/max}$, where $\widetilde{c}_s = \frac{c_s}{c_s^{max}}$ represents the state of lithiation obtained as the ratio between the local c_s and maximum Li concentration c_s^{max} in the active material. The operative states of lithiation for the electrodes are inferred by setting an open circuit voltage of the cell ($V_{oc} = U_{eq,P} - U_{eq,N}$) of 3.42 V for charged state and 2.98 V for discharged state. These V_{oc} values, evaluated after 1 h relaxation following complete charge and discharge, are measured through capacity tests at 25 °C (T_{ref}), while the $U_{eq,ref}$ and EHC (Eqs. (17a)–(17b)) values, used to determine the equilibrium potential of electrode materials at each temperature ($U_{eq,P}$ and $U_{eq,N}$, Eqs. (17c)–(17d)), are sourced from the literature [3,10,92,94]. As a result, the range of operative states of lithiation are evaluated as 0.04–0.73 for the negative electrode and 0.03–0.90 for the positive electrode, which lie within typical ranges reported in the literature [10,78,84,91,92]. By combining the rated specific capacity of 18.21 Ah m^{-2} at C/3, the maximum concentration of Li in the active material c_s^{max} [10,30], the electrode thickness L [51] (Table 1), and the operative state of lithiation range, it is possible to retrieve the volume fraction of the active material ε_{am}. For the positive electrode ε_{am} equals 0.45, while for the negative electrode ε_{am} is adjusted to 0.463 to match the specific capacity of the positive electrode plus a 1 % excess. This adjustment is justified as it reduces the risk of Li plating during charging without significantly impacting the cell energy density [91]. The volume fraction of the pore phase ε_{ey} is then determined as the complement to one. The tortuosity factor of relevant phases is obtained using the Bruggeman relation [65], setting the Bruggeman coefficient $\beta = 1.5$ for all porous composites. From the volume fraction of the active material and the particle radius, the active material particle surface area per unit of volume is calculated as $A_{am} = \frac{3\varepsilon_{am}}{r}$, where r is the average radius of active material particles [51] (Table 1).

The transport properties in the electrolyte, such as the transference number of Li ions t_+, the ionic conductivity σ, the ambipolar diffusivity $\widetilde{D}$, and the electrolyte thermodynamic factor $\gamma_\pm$, are derived from the study by Valoen et al. [95]. Effective electrical conductivity $\sigma_{e,eff}$ values are used for the electrodes [96]. The transport and kinetic properties of the electrode active materials have been fitted to experimental voltage and temperature data from C/2 charge tests at 10, 25, and 40 °C, which have been used as calibration datasets. For the graphite electrode, the diffusion coefficient $\overline{D}_s^{\circ}$ and charge-transfer kinetic constant k_{ct} reference values were derived from previous works where the temperature was held constant at 25 °C, meaning that the activation energies E_{D_s} and $E_{k_{ct}}$ were not determined. Thus, these activation energies have been fitted in this study based on the calibration dataset. For the LFP cathode, the diffusion coefficient D_s° and charge-transfer kinetic constant, along with their respective activation energies, have been entirely fitted to match calibration experimental data. The values obtained for the LFP agree with those reported in previous literature papers [10,84,87,88,90,97]. As a remark, due to the different approach used to model Li transport in the active material, $\overline{D}_s^{\circ}$ and D_s° are fundamentally different: the former represents the intrinsic diffusion coefficient (for graphite) while the latter the chemical diffusion coefficient (for LFP). For more information on this topic, the reader is referred to specific literature papers [70,71,73,98]. Lastly, parameters required for the lumped thermal model, including the effective specific heat c_p and the heat transfer coefficient h, are directly sourced from a previous study on this battery type [51].

Table B2 in Appendix A, along with data in the Supplementary information, summarise the set of geometrical, thermo-electrochemical, and transport parameters used to simulate the graphite-LFP battery.

3. Results

In this section, the ECM and the PBM are extensively calibrated and validated against experimental data derived from electrical tests on the reference graphite/LFP battery, as introduced in Section 2.1. Initially, the ECM and PBM are calibrated through dedicated tests to fine-tune unknown model parameters, providing insights into the required efforts for parameter acquisition (Section 3.1). Subsequently, these calibrated models are subjected to a comprehensive cross-validation process, involving a broader array of electrical tests, including those used during calibration (Section 3.2). This analysis offers a comparative perspective on the predictive discrepancies between the two models, quantifying their advantages and limitations. Furthermore, the practical application of the ECM and PBM is explored in predicting voltage and thermal responses of the battery under the WLTC protocol, thereby evaluating the current trade-offs inherent to each modelling approach. All simulations in this study were conducted using Dymola and COMSOL Multiphysics [99] software for the ECM and PBM, respectively.

3.1. ECM and PBM calibration results

In this section, the ECM and PBM, presented in Sections 2.2 and 2.3, respectively, are calibrated against experimental data derived from dedicated tests. The ECM is calibrated utilising MSTs performed at varying ambient temperatures of 10, 25, and 40 °C (namely test 1 in Table 2). The aim is to extract electrical and thermal equivalent circuital elements as functions of the battery state of charge (SOC) and cell temperature (T), employing the procedure described in Section 2.2. Correspondingly, the PBM is calibrated by fitting the model to experimental data from C/2 charge tests (test 2 in Table 1) at the same three ambient temperatures, addressing the model unknown transport and kinetics related parameters. This process ensures an equivalent number of datasets for the calibration of both models. Specifically, for the ECM, MST is essential as it requires relaxation periods to accurately fit the resistance (R) and capacitance (C) parameters. For the PBM, the choice of using a charge rate of C/2 is strategic as it spans the entire SOC spectrum while providing overpotentials sufficiently large to discriminate between various physical phenomena.

The calibration accuracy is evaluated by comparing the model predictions of voltage and temperature with the corresponding experimental measurements acquired during the electrical tests. For each test the accuracy is quantified using two error indicators: the root mean square error (RMSE) and the maximum absolute error (MAE), as specified in Eqs. (18) and (19). In these equations, the variable X may represent either the battery voltage or temperature, with the subscripts ‘mod’ and ‘exp’ denoting the modelled and experimental values, respectively. The variable N is the total number of datapoints for the test, calculated as the ratio of the test duration to the sampling interval, which in this study is consistently set at one second, aligning with the temporal resolution of the ECM and PBM simulations.

$$RMSE = \sqrt{\sum_{i=1}^{N} \frac{\left(X_{mod,i} - X_{exp,i}\right)^2}{N}} \tag{18}$$

$$MAE = max\left|X_{mod} - X_{exp}\right| \tag{19}$$

The outcomes of the calibration for both models are graphically depicted in Fig. 3. The figure presents a series of subplots (Fig. 3a–f) illustrating the voltage (on the left y-axis) and temperature (on the right y-axis) of the battery over time, demonstrating the performance of the ECM and PBM post-calibration. Fig. 3a–c displays the results for the ECM calibration using 1C MSTs at 10, 25, and 40 °C, while Fig. 3d–f presents the PBM calibration outcomes from C/2 charge tests at the same temperatures. The plots distinguish the datasets with dotted lines for experimental data, solid orange lines for ECM predictions, and dashed blue lines for PBM predictions.

From the analysis of Fig. 3a–c, it is evident that the ECM can accurately reproduce the battery behaviour during MSTs, capturing voltage and temperature profiles across a range of ambient temperatures. The ECM particularly reflects the relaxation phase of each pulse accurately, with only minor and localized deviations noted for the third pulse at 10 °C. The ECM predictions align well with the experimental data during the pulse application phases, and accurately predicts the voltage evolution from mid to high SOC levels. However, at lower SOC levels, the ECM tends to predict a voltage slightly higher than the experimental data, with this disparity being more significant at 10 °C. The agreement between the ECM predictions and experimental data is closer at higher temperatures, especially at 40 °C. The maximum voltage error MAE is obtained at low SOC, registering 288 mV at 10 °C, 187 mV at 25 °C, and 88 mV at 40 °C. The temperature evolution of the battery is also well-captured by the ECM, both during the pulse phase and the subsequent cooling during relaxation. Yet, the ECM tends to overestimate heat generation at higher ambient temperatures, again noticeable at lower SOCs. The maximum temperature MAE is limited, not exceeding 1.6 °C, and is attained at 40 °C. Overall, the ECM offers a satisfactory match with the experimental data, with the highest RMSE values for voltage and temperature constrained to 16 mV (at 10 °C) and 0.4 °C (at 40 °C), respectively. As a final remark, following the execution of MSTs, the parameterization of the ECM includes circuit elements that exhibit only 10 discrete values as a function of SOC, repeated for the 3 temperatures tested (as reported in Fig. A1). This inherently makes the model much

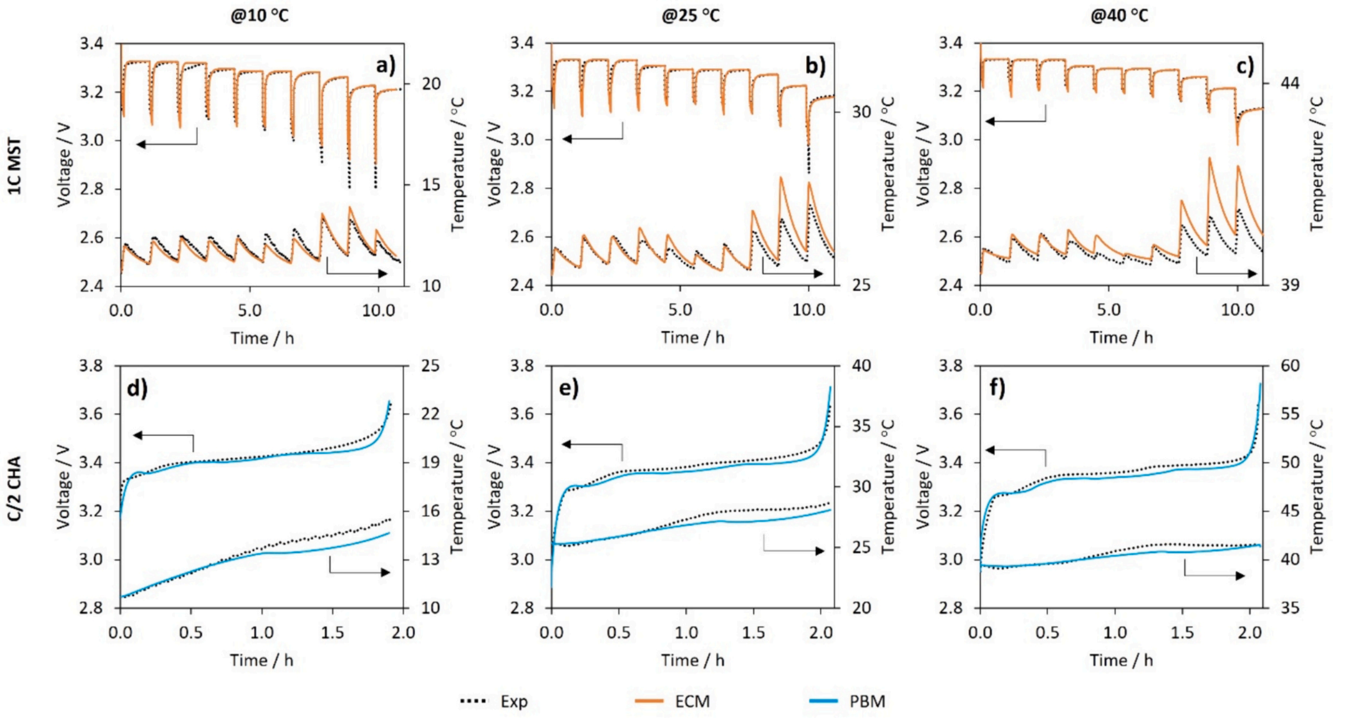

Fig. 3. Calibration results for ECM and PBM across different ambient temperatures. Subplots (a–c) show the ECM performance during MST at 10 °C, 25 °C, and 40 °C, with voltage on the left y-axis and surface temperature on the right, over time. Subplots (d–f) depict the PBM response to C/2 charge tests at the same temperatures. Experimental data (dotted lines), ECM (solid orange), and PBM (solid blue) are compared. (For interpretation of the references to colour in this figure legend, the reader is referred to the web version of this article.)

more accurate under conditions close to the individual points it was calibrated on, while tending to show slight deviations during transitions between these operation points.

The PBM, upon analysis of Fig. 3d–f, also demonstrates an accurate reproduction of battery behaviour during the C/2 charge tests, accurately reflecting the voltage and temperature profiles. The model effectively captures the characteristic voltage curve of the battery, including the plateau-like phases indicative of graphite staging, which are particularly evident in Fig. 3e and f. These voltage plateaus are more discernible at the higher temperatures of 25 and 40 °C; given the low-rate conditions of the C/2 charging, this is attributed to the lower diffusion and kinetic overpotentials at these temperatures, as opposed to the lower temperature of 10 °C, leading to a clearer emergence of the equilibrium fingerprint of graphite staging in the cell signal. The predicted voltage by the PBM is generally lower than the experimental values, likely due to the chosen open circuit voltage function for LFP and the assumption of Fick-like transport within the LFP, which does not account for phase separation. In fact, at lower charge rates and higher temperatures, the equilibrium phenomena are more apparent, resulting in a higher deviation. Such deviations are a consequence of the steepness of the equilibrium potential functions at low and high SOC values, especially for LFP, so that even minor discrepancies in the estimations of the state of lithiation of the active materials escalate to sensible errors in the voltage response. Conversely, at the lower temperature of 10 °C, slower transport in both the solid and electrolyte phases, as well as kinetic resistances, tend to overshadow these equilibrium effects on the cell signal. Here, the PBM aligns more closely with the experimental data during most of the C/2 charge process, except towards the end, where it tends to underestimate the voltage. The MAE in voltage of the PBM remains below 91.8 mV, typically manifesting at the start or the end of charging. The temperature predictions of the PBM at the initial stages of charging are well-aligned with the experimental results; however, slight deviations are observed as the charge progresses. These deviations are linked to the variability in the entropic heat coefficient (EHC) functions sourced from the literature, which exhibit significant variability among different sources, particularly for LFP electrodes [10,84,92,100,101]. This variability profoundly influences the reversible heat generation, which can be either exothermic or endothermic depending on the EHC value, which is comparable to irreversible and ohmic heat sources at such a moderate charge rate. Nevertheless, the MAE for the PBM temperature prediction stays below 1 °C, reinforcing the model robustness in simulating thermal and voltage dynamics. For the PBM, the highest RMSE values for voltage and temperature are 22.8 mV (at 40 °C) and 0.6 °C (at 10 °C), respectively.

3.2. ECM and PBM extended validation

Upon the establishment of the calibration parameters, the ECM and the PBM are subjected to an extended validation process. This rigorous evaluation extends beyond the calibration tests to encompass a broader group of electrical tests, providing a deeper comparative analysis of the models under diverse operational conditions. Such a comprehensive assessment not only highlights the predictive capacities of each model but also assesses their respective limitations and strengths.

The calibrated ECM and PBM are tested against the complete electrical dataset encompassing Tests 1-7, as previously delineated in Section 2.1. This dataset includes MST at 1C, constant current (CC) charge (CHA) at C/2 and 1C, and CC discharge (DCH) tests at C/3, C/2, 1C, and 2C, all conducted at ambient temperatures of 10, 25, and 40 °C. It is noteworthy that this approach permits the evaluation of the PBM with the calibration dataset initially used for the ECM, and vice versa, and additionally with experimental data not used in the calibration of each model.

The accuracy of the models is quantitatively assessed using the RMSE and MAE indicators, as in the previous section, with the results presented in Fig. 4. This figure reports the RMSE (Fig. 4a–c) and MAE (Fig. 4d–f) values for voltage (denoted in red triangles) and temperature (denoted in blue squares) predictions across the varied test conditions at the ambient temperature of 10 °C (Fig. 4a, d), 25 °C (Fig. 4b, e), and 40 °C (Fig. 4c, f). Empty markers show ECM results, whereas filled

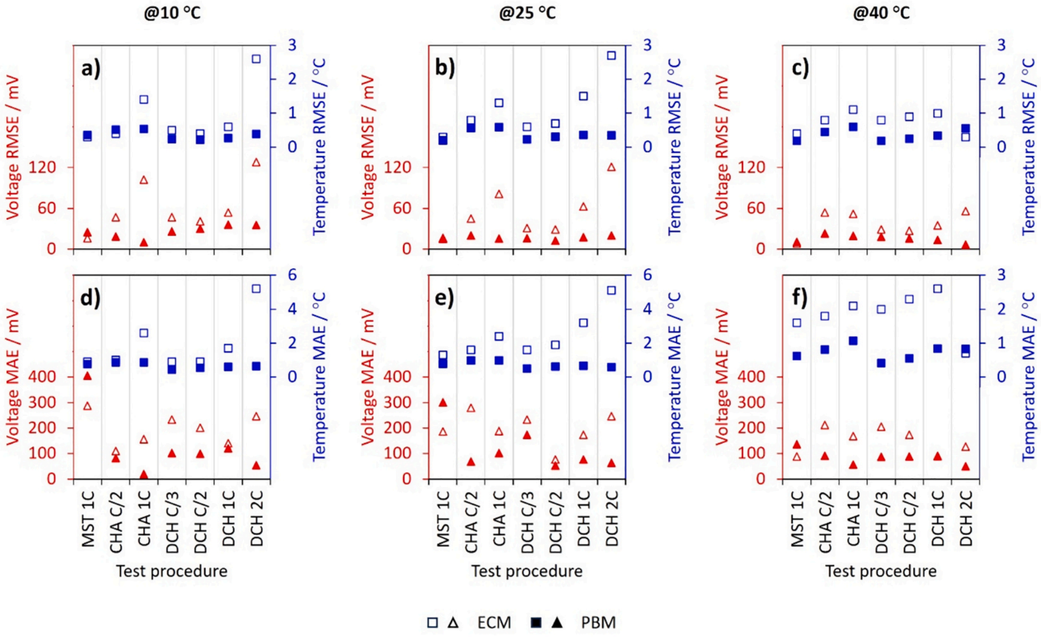

Fig. 4. RMSE (a–c) and MAE (d–f) results for the extended validation of the ECM and PBM for voltage (red) and temperature (blue) predictions at different ambient temperatures 10 °C (a, d), 25 °C (b, e), and 40 °C (c, f). Each subplot reports quantitative indication of the accuracy of model predictions under various operative conditions delineated by tests 1–7 in Table 2. (For interpretation of the references to colour in this figure legend, the reader is referred to the web version of this article.)

markers correspond to PBM results.

From the analysis of Fig. 4, the PBM displays a relatively consistent trend across the test procedures and ambient temperatures, whereas the ECM exhibits more fluctuations. Among the RMSE and MAE metrics for a given model, RMSE values show clearer trends across operational conditions, whereas MAE results do not present discernible patterns, except for temperature predictions. In the case of temperature, both models demonstrate an increase in MAE corresponding to the increase in C-rate for the CHA and DCH procedures. Specifically, as discussed in Section 3.1, the maximum error in temperature is generally located at early or late times where the voltage drop is more pronounced.

For MSTs, in terms of voltage RMSE (red in Fig. 4a–c), the ECM marginally outperforms the PBM at all ambient temperatures, with the difference being more pronounced at 10 °C. This observation remains fairly consistent for temperature RMSE too (blue in Fig. 4a–c). These results are expected, given that the ECM was calibrated specifically on the MST datasets, unlike the PBM. Fig. 5 offers a focus on the simulation results of both the ECM and PBM for battery voltage and temperature during MST at the extremities of the ambient temperature spectrum, specifically at 10 and 40 °C, to cover the entire range of ambient temperature tests.

In terms of voltage predictions, the PBM shows a faster response of the system during relaxation phases, with the voltage rising more rapidly to the corresponding open circuit value, although not always congruent with the experimental data, particularly at the last relaxation phase at 10 °C. Such a faster model response may be associated with a general underestimation of diffusion resistance while the misprediction at the last relaxation at 10 °C is attributed to the variability of the open circuit potential functions of the active materials at extreme states of lithiation. Notably, the PBM more accurately replicates the voltage increase following the third pulse (red arrow in Fig. 5a), which is likely attributable to the staging phenomena of the graphite, an aspect taken into account by the physical model via the phase-field implementation. Regarding temperature prediction, at 10 °C the PBM generally overestimates the cooling during the relaxation phase, while providing better predictions than the ECM during current pulses at medium SOC values. At 40 °C, while the PBM still overestimates the initial cooling, it enables a more accurate prediction at later stages, closely matching the experimental temperature peaks, in contrast to the ECM which tends to overestimate heat generation.

When considering the constant current tests (CHA and DCH procedures), the analysis of Fig. 4 indicates that the PBM yields better results in terms of RMSE and MAE for both voltage and temperature predictions. As expected, given the calibration of the PBM with C/2 constant current charge tests, the ECM exhibits comparatively higher RMSE and MAE values under such conditions. Nonetheless, when tested beyond their respective calibration datasets, the PBM demonstrates a more robust and consistent fit to the experimental data compared to the ECM. Notably, for the ECM both voltage and temperature RMSE values increase significantly with the C-rate, a trend similarly observed with MAE results. Fig. 6 highlights the source of such differences between ECM (solid orange) and PBM (solid blue) predictions, and experimental data (dotted black) during 1C charge (Fig. 6a, b) and discharge (Fig. 6c, d) procedures at two ambient temperatures, 10 °C (Fig. 6a, c) and 40 °C (Fig. 6b, d). These test conditions were selected to provide a thorough understanding of the battery dynamics at a consistent rate and across a significant temperature range to capture the full range of operational behaviours. Voltage profiles are plotted on the left y-axis, while temperature profiles are referenced on the right y-axis.

When examining the voltage predictions, it is evident that the ECM prediction exhibits marked deviations from the experimental data, particularly during the charging phase at 10 °C. The voltage profile predicted by the ECM at this lower temperature not only diverges quantitatively but also presents an unphysical trend. At 40 °C, while the

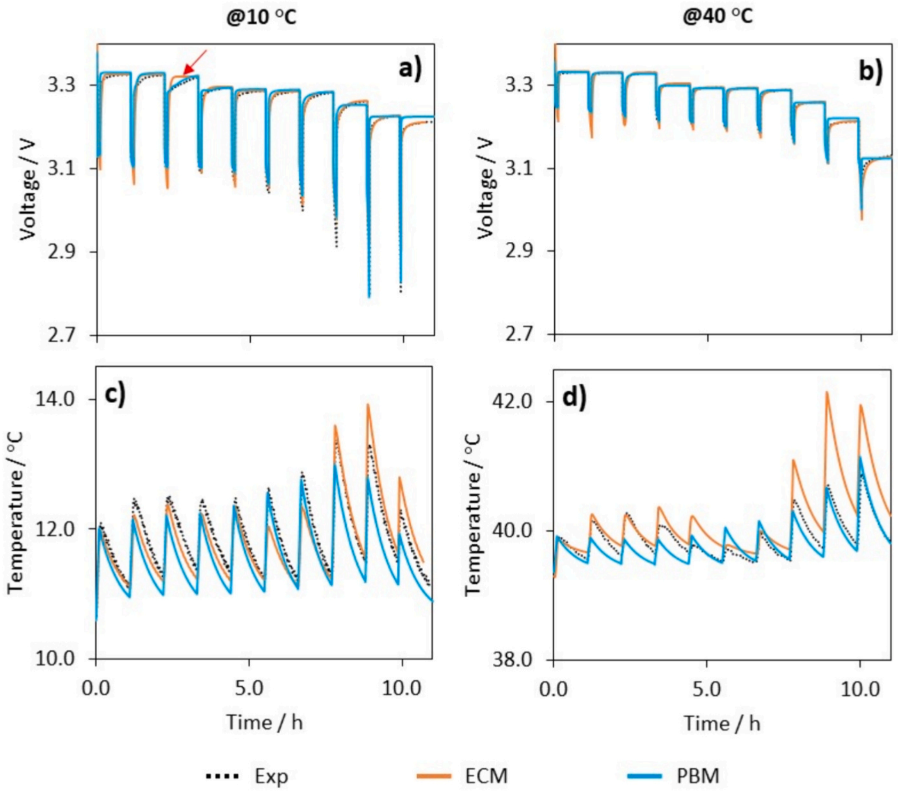

Fig. 5. Performance comparison of ECM and PBM predictions for MSTs at different ambient temperatures at 10 °C (a, c) and 40 °C (b, d). Voltage (a, b) and temperature (c, d) subplots compare experimental data (dotted), and ECM (solid orange) and PBM (solid blue) predictions. (For interpretation of the references to colour in this figure legend, the reader is referred to the web version of this article.)

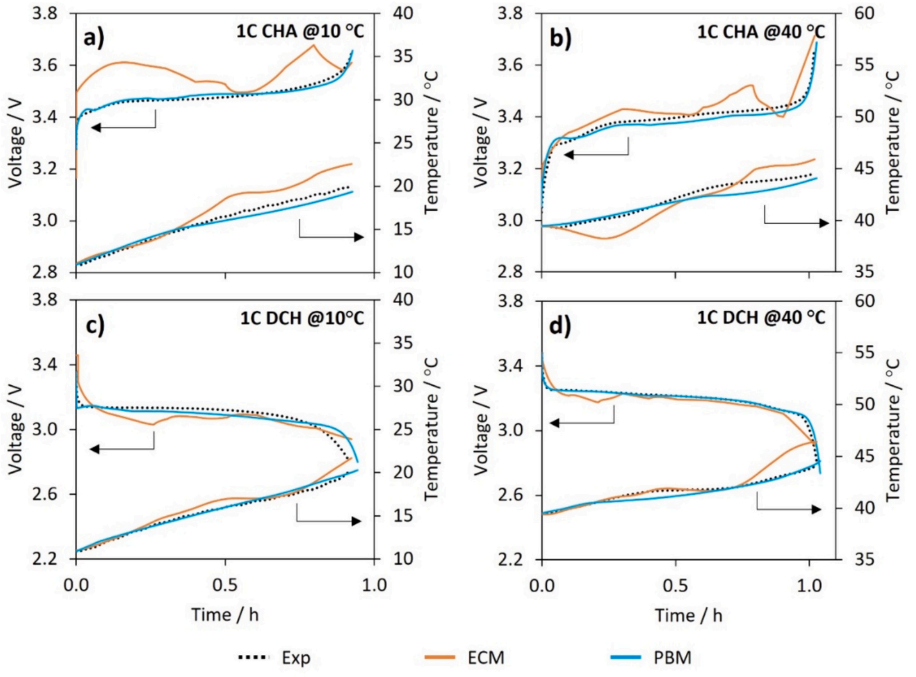

Fig. 6. Performance comparison of ECM (solid orange) and PBM (solid blue) models predictions for charge (a, b) and discharge (c, d) tests at different ambient temperatures of 10 (a, c) and 40 °C (b, d) against experimental data (dotted black). Voltage profiles are shown on the left y-axis while temperature profiles on the right y-axis. (For interpretation of the references to colour in this figure legend, the reader is referred to the web version of this article.)

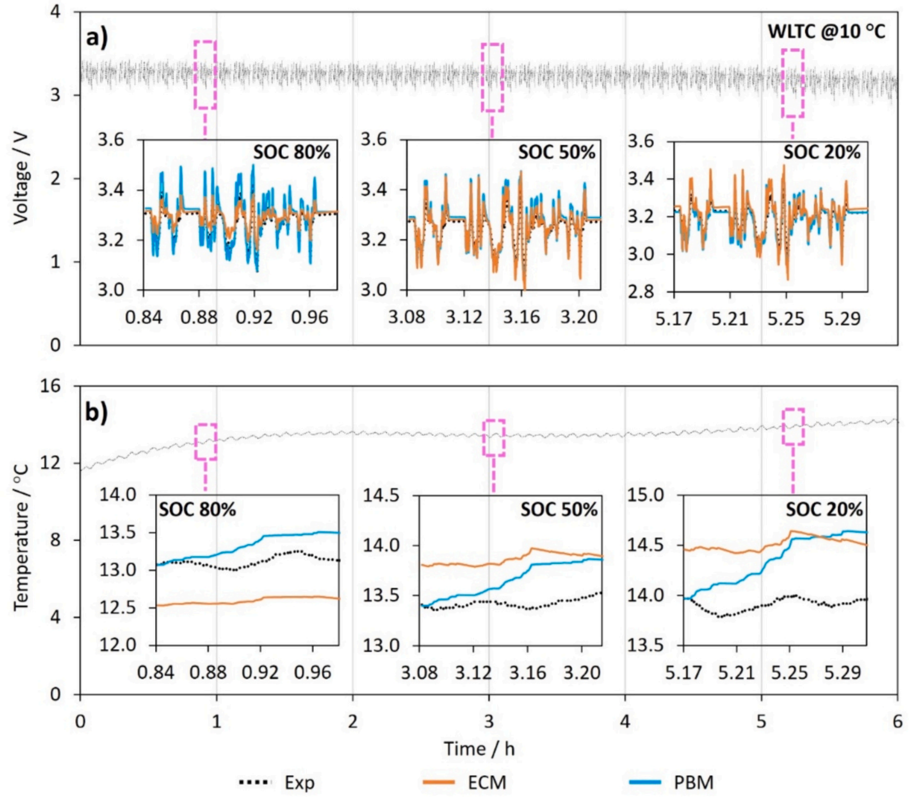

Fig. 7. Comparison between ECM and PBM predictions of WLTC test against experimental data. Voltage (a) and temperature (b) profiles, reporting detailed insets at SOC of 80 %, 50 %, and 20 %, comparing experimental data (dotted) with ECM (solid orange) and PBM (solid blue) predictions. (For interpretation of the references to colour in this figure legend, the reader is referred to the web version of this article.)

deviation in the ECM voltage prediction slightly diminishes, it still maintains a non-monotonic voltage progression during the charge. This behaviour reflects the fact that the parameters of ECM, calibrated from MST single steps only during discharge, are defined only in discrete and limited SOC values, showing in some cases sharp variations with SOC (see Appendix A). During continuous current operations, the SOC variation is wider and the ECM necessarily loses effectiveness. Only during continuous discharge, which is the operation mode used in the MST for ECM calibration, the ECM recovers a fairly satisfactory predictability (Fig. 5c, d). On the other hand, the PBM demonstrates a robust and consistent prediction of the voltage across all tests and ambient temperatures. Its voltage profiles not only align closely to the experimental data but also upholds the physical trends expected during both charge and discharge procedures. This accuracy is indicative of the PBM detailed approach to modelling the battery electrochemical processes, which allows for a more accurate replication of the battery behaviour across varying conditions even beyond the calibration dataset (Figs. S5–8).

Moving on to the analysis of temperature predictions, both models utilise a lumped approach; however, the underlying mechanisms for heat generation rate calculations differ significantly. The PBM calculates heat generation considering specific dynamics of the battery internal components, which results in a more rigorous thermal model. Conversely, the ECM employs a more simplified description of heat generation, which, while capturing the broader trends, lacks the physical interpretation of the PBM approach. Despite these differences, both models generally succeed in following the experimental temperature trends. In all the tests investigated, the battery temperature does not change significantly compared to the ambient temperature, at most increasing by about 10 °C (when the ambient temperature is 10 °C); therefore, it is expected that any plausible thermal model would not give major errors if the tests are nearly isothermal. However, the ECM predictions tend to deviate more from the experimental data, especially at the higher ambient temperature of 40 °C. The PBM, on the other hand, provides consistently more accurate temperature predictions across the range of tests and temperatures, corroborating its comprehensive modelling capabilities.

The extended validation concludes with an evaluation of the ECM and PBM modelling performance under the WLTC test conditions at 10 °C, a temperature that exacerbates prediction errors, as previously discussed. Fig. 7 presents these results, with voltage profiles in Fig. 7a and temperature profiles in Fig. 7b. The experimental data is shown in dotted black lines, while ECM and PBM predictions are reported with solid orange and blue lines, respectively. Insets within Fig. 7 offer a detailed examination of voltage and temperature of the battery at key SOC levels, 80 %, 50 %, and 20 %, underscoring the comparative prediction accuracy between models during repeated WLTC cycles (Fig. S9) until complete battery discharge.

Before discussing the results, it is important to clarify the simulation settings. The PBM required initialisation at each specific SOC (80 %, 50 % and 20 %) and it was run for a single WLTC cycle at each SOC. This is due to its higher computational demands, stemming from the detailed modelling of battery physics, particularly the graphite staging process. Such detailed modelling of graphite lithiation, crucial for accurate predictions, contributes to the extended computation times of the PBM. In contrast, the ECM can simulate the full WLTC within a matter of minutes. The stark contrast is evident as the PBM requires ca. 20 min of computational time for a single WLTC cycle simulation (insets in Fig. 7), representing a 2 % SOC variation in 500 s of real time. The decision to omit the phase separation modelling of LFP in the PBM (see Section 2.3) was a necessary compromise to avoid further computational costs.

Analysing Fig. 7a, both models replicate the WLTC voltage profile, however with notable differences. The ECM predicts the WLTC voltage profile with greater accuracy than the PBM, as indicated by the RMSE and MAE metrics. When comparing the RMSE/MAE values for the voltage, the ECM reports 30.5/101.5 mV against the PBM 37.2/113.5 mV, averaging results from 80 %, 50 %, and 20 % SOC predictions. Notably, the RMSE and MAE values show a trend with SOC levels. For the PBM, RMSE/MAE values incrementally rise from 34.2/102.9 mV at 80 % SOC to 42.3/129.1 mV at 20 % SOC. Similarly, the ECM shows consistent metrics at 80 % and 50 % SOC, with 29.6/88.5 mV and 23.5/84.9 mV respectively, before experiencing a significant increase to 38.4/132.1 mV at 20 % SOC.

At 80 % SOC, the ECM closely matches the experimental data, providing better results than the PBM. However, at lower SOCs, both models exhibit increased deviations from the experimental data, with the PBM showing a consistent trend of overestimating battery voltage during charging peaks and slightly underestimating the voltage during discharging peaks, indicating a general overestimation of internal resistances. A similar trend is observed for the ECM, albeit to a lesser extent and with smaller overshoots at high SOC. Minor variations in predicting the open circuit voltage during relaxation phases are also noted for both models, with the voltage profiles plateauing and exhibiting opposing trends at different SOC levels. While the PBM tends to overestimate voltage during relaxation at high SOC, the ECM predicts higher voltages at low SOC. These minor differences highlight the sensitivity of both models to the equilibrium potential functions they implement, which play a crucial role in their performance.

Further insights into ECM effectiveness in WLTC is gained by examining its RMSE and MAE metrics on the full test. The ECM reports a RMSE value for voltage of 31 mV and a MAE value of 191 mV. Its better performance than PBM in WLTC, as opposed to less robust results in higher current (C-rate $>$ 1) CHA and DCH tests discussed above, is ascribed to two reasons: i) the dynamic nature of the WLTC, which resembles the MST used to calibrate the ECM, and ii) the ranges of charge/discharge currents within the WLTC, which are relatively small in terms of equivalent C-rate. As for the first reason, it is reasonable to presume that the ECM can maintain good predictability when tested in a condition similar to the MST used for its calibration; broadly speaking, both MST and WLTC comprise sudden changes in current and no current phases, thus sharing a similar dynamic nature. Regarding the second reason, a critical factor for the ECM success in WLTC is the applied current rates and respective times. In fact, during the WLTC the average discharge C-rate is 0.49C (dashed red Fig. S9), while the average charging C-rate is 0.34C (dashed green Fig. S9). For the ECM, the RMSE and MAE values obtained during the WLTC are consistent with the RMSE and MAE results for DCH and CHA tests at 0.5C and C/3 presented in Fig. 4. These rates ensure that WLTC operating conditions do not reach the high currents that would challenge ECM predictive accuracy, along with the fact that, when the applied C-rate is larger than 1C in the WLTC, the application time is very short (less than a few seconds, see Fig. S9). This explains the ECM robust performance in WLTC, as it operates within current rates and times that avoid the accuracy loss shown in Figs. 4 and 6. From a quantitative comparison perspective regarding the ECM results, it is reported that the average RMSE obtained from the ECM on dynamic WLTC validation cycles is 25 mV. This value is entirely consistent with the research findings as in [102], which show a range of voltage RMSE values obtained from ECMs for lithium batteries using different calibration methodologies, applied to various dynamic working cycles comparable to the WLTC, ranging from around 20 to 70 mV.

When analysing Fig. 7b, the different settings of ECM and PBM in simulating WLTC become evident. The PBM simulates only portions of the WLTC, initialising each cycle (i.e., at 80 %, 50 %, 20 % SOC) with the experimental temperature at that specific time, effectively resetting its temperature history. In contrast, the ECM simulates the entire WLTC, potentially carrying a temperature offset derived from the prior history of the WLTC segments shown in the figure. Given this context, a fair comparison of the two model predictions must focus on the trend of temperature change, rather than on absolute values. The ECM predicts these temperature trends more accurately despite potential offsets, while the PBM tends to overestimate heat generation. This suggests an overprediction of internal resistances, as already noted for the voltage peaks, leading to higher generated heat. Under these premises, the ECM provides a comparatively better prediction of the temperature trend during the WLTC. In any case, it must be observed that the magnitude of temperature deviations is small and, overall, the cell temperature remains relatively invariant during the WLTC.

Hence, while the ECM may not always offer the most precise predictions in charge and discharge cycles (Fig. 4), it balances computational efficiency with a reasonable predictive accuracy under operating conditions with variable current pulses. This balance renders the ECM particularly suitable for real-time assessments of voltage and temperature behaviours, particularly in dynamic scenarios like WLTC. The ECM effectively manages high C-rates, peaking briefly at around 1.9C (6 s), when each current load, whether charging or discharging, is applied for no >10 s (Fig. S9). This is a crucial factor in the ECM performance since the model is best suited for predictions in dynamic protocols with good accuracy when the current loads are either sufficiently low or, in cases of higher current, the pulses are of short duration. Such conditions are met during the WLTC tests, but it is important to note that these conditions might not always align with real-world applications where current demands and profiles can vary significantly, such as during continuous and fast charging or for prolonged discharging (e.g., when driving an EV in a highway or for steady energy supply from a battery to the grid), for which the PBM must be preferred.

4. Conclusion

In this study, a thorough comparison between the Equivalent Circuit Model (ECM) and the Physics-Based Model (PBM) has been conducted within the context of Li-ion battery modelling, targeting a 60 Ah prismatic graphite/lithium-iron-phosphate battery as a case study.

A comprehensive series of tests, including various electrical protocols (i.e., variable and constant currents from C/3 to 2C) and temperature conditions (from 10 to 40 °C), revealed the operational strengths and limitations of both models. The validation of these models is crucial to the findings, with an average error in voltage predictions across the ambient temperature range of 51.5 mV for the ECM and 19.3 mV for the PBM. For temperature predictions, the average errors were 0.9 °C for the ECM and 0.4 °C for the PBM. These measures of accuracy demonstrate the reliability of both models under the tested conditions.

The findings of this study indicate that the ECM is particularly effective in dynamic scenarios like the WLTC, offering rapid computational response and reasonable accuracy within its calibration range, especially for low to medium current intensities without prolonged charging current pulses. However, its limitations under high current demands, where its predictive accuracy diminishes, underline the need for a more comprehensive model. Conversely, the PBM provides a more detailed representation of battery physics, making it more suitable and robust for in-depth analysis of battery behaviour, particularly in scenarios involving high-rate operation, as well as in working conditions close to SOC extreme values (i.e., 100 and 0 %), where the ECM lacks robustness. Despite its time-intensive calibration process and longer computation times, the PBM strengths in accurately modelling high-rate operations render it indispensable for research purposes and for optimisation, including fast charging protocols.

In conclusion, the practical application of battery modelling requires a considered selection between ECM and PBM based on the specific demands of the task at hand. ECM and PBM represent complementary tools: advancing these models in tandem will enable their application across a diverse range of scenarios, ensuring that both rapid, efficient performance assessments and thorough, in-depth investigations into battery behaviour are effectively addressed.

CRediT authorship contribution statement

Marco Lagnoni: Writing – review & editing, Writing – original draft, Visualization, Validation, Software, Methodology, Investigation, Formal analysis, Data curation, Conceptualization. **Claudio Scarpelli:** Writing – review & editing, Writing – original draft, Validation, Software, Methodology, Investigation, Formal analysis, Data curation, Conceptualization. **Giovanni Lutzemberger:** Writing – review & editing, Supervision, Resources, Project administration, Methodology, Conceptualization. **Antonio Bertei:** Writing – review & editing, Supervision, Resources, Project administration, Methodology, Funding acquisition, Conceptualization.

Declaration of competing interest

The authors declare that they have no known competing financial interests or personal relationships that could have appeared to influence the work reported in this paper.

Data availability

Data will be made available on request.

Acknowledgments

M.L. and A.B. acknowledge funding from the Ministero dell'Università e della Ricerca (MUR) - European Union NextGenerationEU - National Recovery and Resilience Plan (NRRP) - MISSION 4 COMPONENT 2, INVESTMENT N. 1.3 - CUP N. I53C22001450006, within the project Network 4 Energy Sustainable Transition (NEST). This manuscript reflects only the authors' views and opinions, neither the European Union nor the European Commission can be considered responsible for them.

Appendix A

Appendix A presents a comprehensive graphical overview of the Equivalent Circuit Model (ECM) parameters that were determined during the calibration activities described in Section 3.1. These visual representations are crucial for a deeper understanding of the ECM behaviour under various operational conditions. They serve as an essential complement to the numerical data provided, offering a more intuitive grasp of the parameter variations and trends. For readers interested in the precise numerical values of these ECM parameters, Table S2 and S3 in the Supplementary information provide detailed tabulations.

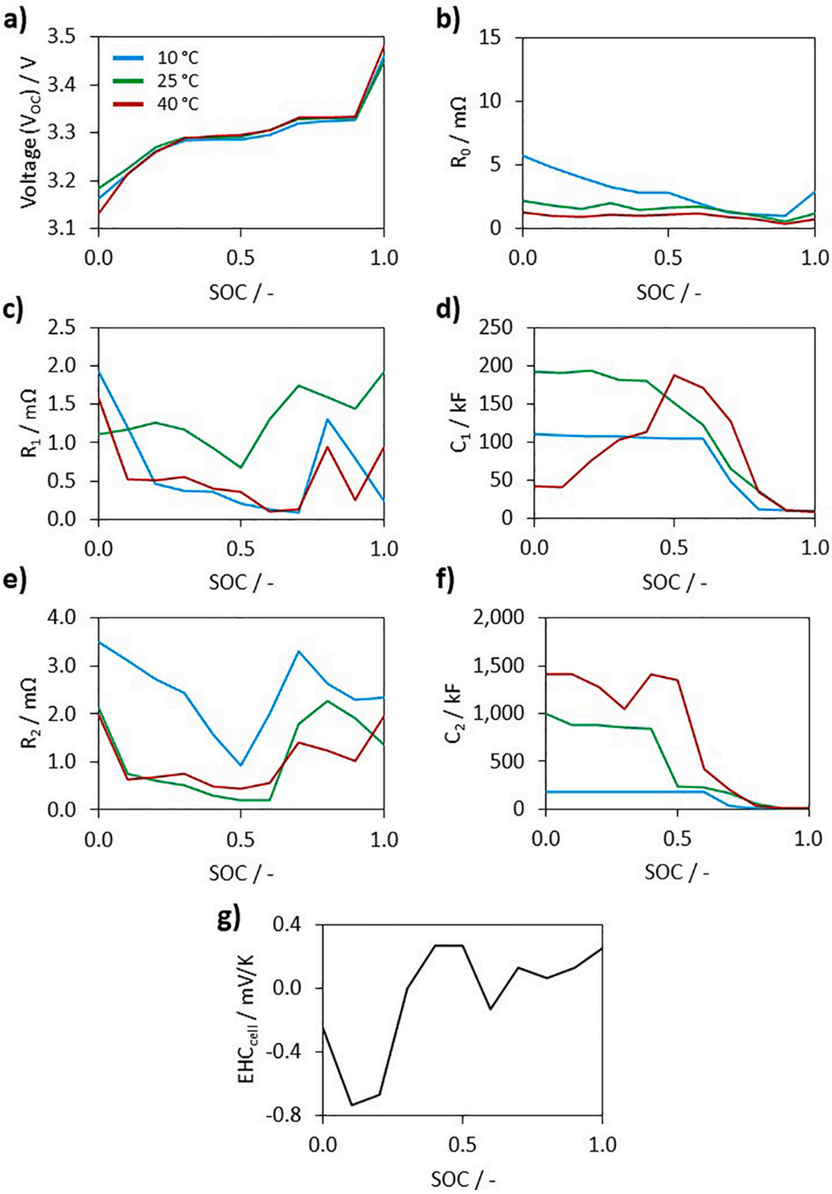

Fig. A1. ECM parameters dependency with the state of charge (SOC) and temperature. This figure illustrates the dependencies of key ECM components: open circuit voltage of the cell V_{oc} (a), resistance R_0 (b), resistance R_1 (c), capacitance C_1 (d), resistance R_2 (e), capacitance C_2 (f), at different temperatures: 10 °C (blue), 25 °C (green), and 40 °C (red). Panel (g) presents a linear interpolation depicting the relationship between V_{oc} and ambient temperature changes.

Appendix B

Appendix B includes the boundary conditions (Table B1) and parameterisation (Table B2) for the physics-based model (PBM) detailed in Section 2.3. Table B1 reports the model boundary condition. Table B2 reports the parameterisation outcomes from the calibration activities discussed in Section 3.1. Additionally, specific functions and datasets reported in Table B2 are included in the PBM-dedicated section of the Supplementary information.

Table B1
Boundary conditions of the PBM.

Balance of mass – *ey* phase (Eq. (10a))	$J_{conc}\big\|_{x=I} = 0; J_{conc}\big\|_{x=IV} = 0$
Balance of charge – *ey* phase (Eq. (11a))	$J_2\big\|_{x=I} = 0; J_2\big\|_{x=IV} = 0$
Balance of charge – *el* phase (Eq. (12a))	$\widetilde{\mu}^*_{e,N}\Big\|_{x=I} = 0; J_{1,N}\big\|_{x=II} = 0$ $J_{1,P}\big\|_{x=IV} = \frac{i_{cell}}{N_{cell}A_{act}}\ (CC)$ $J_{1,P}\big\|_{x=III} = 0;$ $\widetilde{\mu}^*_{e,P}\Big\|_{x=IV} = V_{CV}\ (CV)$
Balance of mass – *s* phase (Eq. (13a))	$J_{s,i}\big\|_{y=0} = 0; J_{s,i}\big\|_{y=r_i} = J_{ct,i}$

Table B2

Geometrical, microstructural, electrochemical and transport parameters of the PBM.

Parameter	Negative electrode (graphite)	Separator	Positive electrode (LFP)
Thickness L/[µm]	72.5[a]	25[a]	76.1[a]
Particle radius r/[µm]	10[b] [3]		0.0365[b] [51,103]
Active material surface area per unit of volume A_{am}/[m^{-1}]	$1.376\ 10^{5}$[c]		$3.699\ 10^{7}$[c]
Volume fraction ε/[–]	$am = el = 0.463$[c] $fill = 0.057$[b] [93] $ey = 0.480$[c]	$fill = 0.55$[c] $ey = 0.45$[b] [78]	$am = 0.450$[c] $fill + el = 0.1$[b] [91] $ey = 0.450$[c]
Bruggeman factor β/[–]	←	1.5[b] [83]	→
Symmetry factor α/[–]	0.5[b]		0.5[b]
Kinetic constant k_{ct}°/[A m^{-2}]	Table S6[d]		Table S6[d]
Maximum Li concentration c_s^{max}/[mol m^{-3}]	29,920[b] [30]		22,806[b] [10,103]
Open circuit potential U_{eq}/[V]	Eqs. (S1a)–(S1g)[b] [3]		Eq. (S2)[b] [92]
Characteristic interface length a/[µm]	0.316[b] [3]		–
Standard potential of intercalated Li E°/[V]	0.136[b] [3]		–
Entropic heat coefficient EHC/[V K^{-1}]	Table S4[b] [68]		Table S5[b] [100]
Min/Max state of lithiation $\tilde{c}_s^{min/max}$/[–]	Min = 0.04[b] Max = 0.73[b]		Min = 0.03[b] Max = 0.90[b]
Solid-phase conductivity σ_{el}/[S m^{-1}]	10[b] [3]		6.75[b] [96]
Solid-phase diffusivity $D_s^{\circ}/\overline{D}_s^{\circ}$/[m^2 s^{-1}]	Table S7[d] [3]		Table S8[d]
Charge-transfer constant activation energy $E_{k_{ct,i}}$/[J mol^{-1}]	20,000[d]		30,000[d]
Solid-phase diffusion activation energy $E_{D_{s,i}}$/[J mol^{-1}]	45,000[d]		50,000[d]
Initial electrolyte concentration c^{in}/[mol m^{-3}]	←	1000[b] [78]	→
Transference number of positive charges t_+/[–]	←	0.38[b] [95]	→
Ambipolar diffusivity $\widetilde{D}$/[m^2 s^{-1}]	←	Eq. (S3)[b] [95]	→
Ionic conductivity σ/[S m^{-1}]	←	Eq. (S4)[b] [95]	→
Thermodynamic factor $\gamma_{\pm}$/[–]	←	Eq. (S5)[b] [95]	→
Heat transfer coefficient h/[W m^{-2} K^{-1}]		20[a] [51]	
Equivalent specific heat c_p/[J kg^{-1} K^{-1}]		1600[a] [51]	

[a] Measured.

[b] Assumed.

[c] Calculated.

[d] Fitted to experimental data.

Appendix C. Supplementary data

Supplementary data to this article can be found online at https://doi.org/10.1016/j.est.2024.112326.

References

[1] R. Schmuch, R. Wagner, G. Hörpel, T. Placke, M. Winter, Performance and cost of materials for lithium-based rechargeable automotive batteries, Nat. Energy 3 (2018) 267–278, https://doi.org/10.1038/s41560-018-0107-2.

[2] S.F. Tie, C.W. Tan, A review of energy sources and energy management system in electric vehicles, Renew. Sust. Energ. Rev. 20 (2013) 82–102, https://doi.org/10.1016/j.rser.2012.11.077.

[3] X. Lu, M. Lagnoni, A. Bertei, S. Das, R.E. Owen, Q. Li, K. O'Regan, A. Wade, D. P. Finegan, E. Kendrick, M.Z. Bazant, D.J.L. Brett, P.R. Shearing, Multiscale dynamics of charging and plating in graphite electrodes coupling operando microscopy and phase-field modelling, Nat. Commun. 14 (2023) 5127, https://doi.org/10.1038/s41467-023-40574-6.

[4] X. Lu, X. Zhang, C. Tan, T.M.M. Heenan, M. Lagnoni, K. O'Regan, S. Daemi, A. Bertei, H.G. Jones, G. Hinds, J. Park, E. Kendrick, D.J.L. Brett, P.R. Shearing, Multi-length scale microstructural design of lithium-ion battery electrodes for improved discharge rate performance, Energy, Environ. Sci. 14 (2021) 5929–5946, https://doi.org/10.1039/d1ee01388b.

[5] H. Zhao, B.D. Storey, R.D. Braatz, M.Z. Bazant, Learning the physics of pattern formation from images, in: AIChE Annual Meeting, Conference Proceedings, American Institute of Chemical Engineers, 2020, https://doi.org/10.1103/PhysRevLett.124.060201.

[6] M.Z. Bazant, Unified quantum theory of electrochemical kinetics by coupled ion–electron transfer, Faraday Discuss. (2023), https://doi.org/10.1039/d3fd00108c.

[7] F. Brosa Planella, W. Ai, A.M. Boyce, A. Ghosh, I. Korotkin, S. Sahu, V. Sulzer, R. Timms, T.G. Tranter, M. Zyskin, S.J. Cooper, J.S. Edge, J.M. Foster, M. Marinescu, B. Wu, G. Richardson, A continuum of physics-based lithium-ion battery models reviewed, Progress, Energy 4 (2022), https://doi.org/10.1088/2516-1083/ac7d31.

[8] X. Zhang, W. Zhang, G. Lei, A review of li-ion battery equivalent circuit models, Trans. Electr. Electron. Mater. 17 (2016) 311–316. https://api.semanticscholar.org/CorpusID:41459852.

[9] C. Parthasarathy, H. Laaksonen, P. Halagi, Characterisation and Modelling Lithium Titanate Oxide Battery Cell By Equivalent Circuit Modelling Technique, in: 2021 IEEE PES Innovative Smart Grid Technologies - Asia (ISGT Asia), 2021, pp. 1–5. https://api.semanticscholar.org/CorpusID:247108553.

[10] M. Mastali, M. Farkhondeh, S. Farhad, R.A. Fraser, M. Fowler, Electrochemical modeling of commercial LiFePO4 and graphite electrodes: kinetic and transport properties and their temperature dependence, J. Electrochem. Soc. 163 (2016) A2803, https://doi.org/10.1149/2.1151613jes.

[11] M. Xu, Z. Zhang, X. Wang, L. Jia, L. Yang, Two-dimensional electrochemical–thermal coupled modeling of cylindrical LiFePO4 batteries, J. Power Sources 256 (2014) 233–243, https://doi.org/10.1016/j.jpowsour.2014.01.070.

[12] G. Richardson, J. Foster, R. Ranom, C. Please, A. Ramos, Charge transport modelling of lithium-ion batteries, Eur. J. Appl. Math. 33 (2021) 1–49, https://doi.org/10.1017/S0956792521000292.

[13] J. Jamnik, J. Maier, Generalised equivalent circuits for mass and charge transport: chemical capacitance and its implications, Phys. Chem. Chem. Phys. 3 (2001) 1668–1678, https://doi.org/10.1039/b100180i.

[14] M.P. Bonkile, Y. Jiang, N. Kirkaldy, V. Sulzer, R. Timms, H. Wang, G. Offer, B. Wu, Coupled electrochemical-thermal-mechanical stress modelling in composite silicon/graphite lithium-ion battery electrodes, J Energy Storage 73 (2023) 108609, https://doi.org/10.1016/j.est.2023.108609.

[15] G. Galuppini, M.D. Berliner, H. Lian, D. Zhuang, M.Z. Bazant, R.D. Braatz, Efficient computation of safe, fast charging protocols for multiphase lithium-ion batteries: a lithium iron phosphate case study, J. Power Sources 580 (2023) 233272, https://doi.org/10.1016/j.jpowsour.2023.233272.

[16] M.P. Bonkile, V. Ramadesigan, Power management control strategy using physics-based battery models in standalone PV-battery hybrid systems, J Energy Storage 23 (2019) 258–268, https://doi.org/10.1016/j.est.2019.03.016.

[17] R.O. Nemeş, S.M. Ciornei, M. Ruba, C.S. Martis, Parameters identification using experimental measurements for equivalent circuit lithium-ion cell models, in: 2019 11th International Symposium on Advanced Topics in Electrical Engineering (ATEE), 2019, pp. 1–6. https://api.semanticscholar.org/CorpusID:171095755.

[18] T. Kalogiannis, M. Hosen, M.A. Sokkeh, S. Goutam, J. Jaguemont, L. Jin, G. Qiao, M. Berecibar, J. Van Mierlo, Comparative study on parameter identification methods for dual-polarization lithium-ion equivalent circuit model, Energies 12 (2019) 1–37. https://api.semanticscholar.org/CorpusID:208760197.

[19] M.K. Tran, A. Dacosta, A. Mevawalla, S. Panchal, M. Fowler, Comparative study of equivalent circuit models performance in four common lithium-ion batteries:

LFP, NMC, LMO, NCA, Batteries 7 (2021), https://doi.org/10.3390/batteries7030051.

[20] L. Wildfeuer, P. Gieler, A. Karger, Combining the distribution of relaxation times from EIS and time-domain data for parameterizing equivalent circuit models of lithium-ion batteries, Batteries 7 (2021), https://doi.org/10.3390/batteries7030052.

[21] B. Sun, X. He, W. Zhang, H. Ruan, X. Su, J. Jiang, Study of parameters identification method of Li-ion battery model for EV power profile based on transient characteristics data, IEEE Trans. Intell. Transp. Syst. 22 (2021) 661–672, https://doi.org/10.1109/TITS.2020.3032447.

[22] M. Ceraolo, G. Lutzemberger, D. Poli, C. Scarpelli, Model parameter evaluation for nickel-manganese-cobalt cells: an examination and verification of various approaches, IEEE Ind. Appl. Mag. 27 (2021) 29–36, https://api.semanticscholar.org/CorpusID:236734541.

[23] D. Mitra, S. Mukhopadhyay, UKF based estimation of SOC and core temperature of a lithium ion cell using an electrical cell model, in: 2018 15th IEEE India Council International Conference (INDICON), 2018: pp. 1–6. doi:https://doi.org/10.1109/INDICON45594.2018.8987074.

[24] S.S. Madani, E. Schaltz, S.K. Kær, A review of different electric equivalent circuit models and parameter identification methods of lithium-ion batteries, ECS Trans. 87 (2018) 23, https://doi.org/10.1149/08701.0023ecst.

[25] W. Lai, F. Ciucci, Mathematical modeling of porous battery electrodes-Revisit of Newman's model, Electrochim. Acta 56 (2011) 4369–4377, https://doi.org/10.1016/j.electacta.2011.01.012.

[26] M. Doyle, J. Newman, The use of mathematical modeling in the design of lithium/polymer battery systems, Electrochim. Acta 40 (1995) 2191–2196, https://doi.org/10.1016/0013-4686(95)00162-8.

[27] J. Newman, W. Tiedemann, Porous-electrode theory with battery applications, AICHE J. 21 (1975) 25–41, https://doi.org/10.1002/aic.690210103.

[28] D. Bernardi, E. Pawlikowski, J. Newman, A general energy balance for battery systems, J. Electrochem. Soc. 132 (1985) 5–12.

[29] E. Prada, D. Di Domenico, Y. Creff, J. Bernard, V. Sauvant-Moynot, F. Huet, Simplified electrochemical and thermal model of LiFePO4-graphite Li-ion batteries for fast charge applications, J. Electrochem. Soc. 159 (2012) A1508, https://doi.org/10.1149/2.064209jes.

[30] S. Ahn, M. Lagnoni, Y. Yuan, A. Ogarev, E. Vavrinyuk, G. Voynov, E. Barrett, A. Pelli, A. Atrashchenko, A. Platonov, S. Gurevich, M. Gorokhov, D. Rupasov, A. W. Robertson, R.A. House, L.R. Johnson, A. Bertei, D.V. Chernyshov, Chemical origins of a fast-charge performance in disordered carbon anodes, ACS Appl Energy Mater (2023), https://doi.org/10.1021/acsaem.3c01280.

[31] D.P. Finegan, A. Quinn, D.S. Wragg, A.M. Colclasure, X. Lu, C. Tan, T.M. M. Heenan, R. Jervis, D.J.L. Brett, S. Das, T. Gao, D.A. Cogswell, M.Z. Bazant, M. Di Michiel, S. Checchia, P.R. Shearing, K. Smith, Spatial dynamics of lithiation and lithium plating during high-rate operation of graphite electrodes, Energy, Environ. Sci. 13 (2020) 2570–2584, https://doi.org/10.1039/d0ee01191f.

[32] Y. Lai, S. Du, L. Ai, L. Ai, Y. Cheng, Y. Tang, M. Jia, Insight into heat generation of lithium ion batteries based on the electrochemical-thermal model at high discharge rates, Int. J. Hydrog. Energy 40 (2015) 13039–13049, https://doi.org/10.1016/j.ijhydene.2015.07.079.

[33] G. Galuppini, M.D. Berliner, D.A. Cogswell, D. Zhuang, M.Z. Bazant, R.D. Braatz, Nonlinear identifiability analysis of multiphase porous electrode theory-based battery models: a lithium iron phosphate case study, J. Power Sources 573 (2023) 233009, https://doi.org/10.1016/j.jpowsour.2023.233009.

[34] J. Kleiner, L. Komsiyska, G. Elger, C. Endisch, Thermal modelling of a prismatic lithium-ion cell in a battery electric vehicle environment: influences of the experimental validation setup, Energies 13 (2020), https://doi.org/10.3390/en13010062.

[35] A. Tang, L. Yao, P. Gong, Y. Jiang, Lithium-ion battery state-of-charge estimation of an order-reduced physics-based model in electric vehicles considering erroneous initialization, Int. J. Energy Res. 46 (2022) 3529–3538, https://doi.org/10.1002/er.7403.

[36] V.R. Subramanian, V. Boovaragavan, V.D. Diwakar, Toward real-time simulation of physics based Lithium-ion battery models, Electrochem. Solid-State Lett. 10 (2007) A255, https://doi.org/10.1149/1.2776128.

[37] R. Scipioni, P.S. Jørgensen, C. Graves, J. Hjelm, S.H. Jensen, A physically-based equivalent circuit model for the impedance of a LiFePO 4/graphite 26650 cylindrical cell, J. Electrochem. Soc. 164 (2017) A2017–A2030, https://doi.org/10.1149/2.1071709jes.

[38] Y. Li, M. Vilathgamuwa, T. Farrell, S.S. Choi, N.T. Tran, J. Teague, A physics-based distributed-parameter equivalent circuit model for lithium-ion batteries, Electrochim. Acta 299 (2019) 451–469, https://doi.org/10.1016/j.electacta.2018.12.167.

[39] Y. Merla, B. Wu, V. Yufit, R.F. Martinez-Botas, G.J. Offer, An easy-to-parameterise physics-informed battery model and its application towards lithium-ion battery cell design, diagnosis, and degradation, J. Power Sources 384 (2018) 66–79, https://doi.org/10.1016/j.jpowsour.2018.02.065.

[40] Z. Geng, S. Wang, M.J. Lacey, D. Brandell, T. Thiringer, Bridging physics-based and equivalent circuit models for lithium-ion batteries, Electrochim. Acta 372 (2021), https://doi.org/10.1016/j.electacta.2021.137829.

[41] H. Pang, J. Jin, L. Wu, F. Zhang, K. Liu, A comprehensive physics-based equivalent-circuit model and state of charge estimation for lithium-ion batteries, J. Electrochem. Soc. 168 (2021) 90552, https://doi.org/10.1149/1945-7111/ac2701.

[42] P. Rodríguez-Iturriaga, D. Anseán, S. Rodríguez-Bolívar, V.M. García, M. González, J.A. López-Villanueva, Modeling current-rate effects in lithium-ion batteries based on a distributed, multi-particle equivalent circuit model, Appl. Energy 353 (2024), https://doi.org/10.1016/j.apenergy.2023.122141.

[43] P. Rodríguez-Iturriaga, D. Anseán, S. Rodríguez-Bolívar, M. González, J.C. Viera, J.A. López-Villanueva, A physics-based fractional-order equivalent circuit model for time and frequency-domain applications in lithium-ion batteries, J Energy Storage 64 (2023), https://doi.org/10.1016/j.est.2023.107150.

[44] R. Tian, S.H. Park, P.J. King, G. Cunningham, J. Coelho, V. Nicolosi, J. N. Coleman, Quantifying the factors limiting rate performance in battery electrodes, Nat. Commun. 10 (2019), https://doi.org/10.1038/s41467-019-09792-9.

[45] J.S. Edge, S. O'Kane, R. Prosser, N.D. Kirkaldy, A.N. Patel, A. Hales, A. Ghosh, W. Ai, J. Chen, J. Yang, S. Li, M.C. Pang, L. Bravo Diaz, A. Tomaszewska, M. W. Marzook, K.N. Radhakrishnan, H. Wang, Y. Patel, B. Wu, G.J. Offer, Lithium ion battery degradation: what you need to know, Phys. Chem. Chem. Phys. 23 (2021) 8200–8221, https://doi.org/10.1039/d1cp00359c.

[46] P. Bai, D.A. Cogswell, M.Z. Bazant, Suppression of phase separation in LiFePO4 nanoparticles during battery discharge, Nano Lett. 11 (2011) 4890–4896, https://doi.org/10.1021/nl202764f.

[47] S. Das, P.M. Attia, W.C. Chueh, M.Z. Bazant, Electrochemical kinetics of SEI growth on carbon black: part II, Modeling, J Electrochem Soc 166 (2019) E107–E118, https://doi.org/10.1149/2.0241904jes.

[48] H. Tu, S. Moura, Y. Wang, H. Fang, Integrating physics-based modeling with machine learning for lithium-ion batteries, Appl Energy 329 (2023) 120289, https://doi.org/10.1016/j.apenergy.2022.120289.

[49] Y. Liang, A. Emadi, O. Gross, C. Vidal, M. Canova, S. Panchal, P.J. Kollmeyer, M. Naguib, F. Khanum, A comparative study between physics, electrical and data driven lithium-ion battery voltage modeling approaches, in: SAE Technical Paper Series, 2022. https://api.semanticscholar.org/CorpusID:248007539.

[50] M. Ben-Marzouk, S. Pelissier, G. Clerc, A. Sari, P. Venet, Generation of a real-life battery usage pattern for electrical vehicle application and aging comparison with the WLTC profile, IEEE Trans. Veh. Technol. 70 (2021) 5618–5627, https://doi.org/10.1109/TVT.2021.3077671.

[51] M. Lagnoni, C. Scarpelli, F. Barontini, A. Bertei, G. Lutzemberger, M. Puccini, Calibration and validation of equivalent circuit and physics-based models for Li-ion battery, in: 2022 AEIT International Annual Conference (AEIT), 2022, pp. 1–6, https://doi.org/10.23919/AEIT56783.2022.9951802.

[52] M. Barbieri, M. Ceraolo, G. Lutzemberger, C. Scarpelli, An electro-thermal model for LFP cells: calibration procedure and validation, Energies 15 (2022) 2653. https://api.semanticscholar.org/CorpusID:247992108.

[53] A.A. Kebede, T. Kalogiannis, J. Van Mierlo, M. Berecibar, A comprehensive review of stationary energy storage devices for large scale renewable energy sources grid integration, Renew. Sust. Energ. Rev. 159 (2022) 112213, https://doi.org/10.1016/j.rser.2022.112213.

[54] C.K. Das, O. Bass, G. Kothapalli, T.S. Mahmoud, D. Habibi, Overview of energy storage systems in distribution networks: placement, sizing, operation, and power quality, Renew. Sust. Energ. Rev. 91 (2018) 1205–1230, https://doi.org/10.1016/j.rser.2018.03.068.

[55] M. Barbieri, M. Ceraolo, G. Lutzemberger, C. Scarpelli, T. Pesso, M. Giovannucci, Simplified electro-thermal model for lithium cells based on experimental tests, in: 2020 AEIT International Conference of Electrical and Electronic Technologies for Automotive (AEIT AUTOMOTIVE), 2020, pp. 1–6. https://api.semanticscholar.org/CorpusID:230996979.

[56] M. Chen, G.A. Rincon-Mora, Accurate electrical battery model capable of predicting runtime and I-V performance, IEEE Transactions on Energy Conversion 21 (2006) 504–511, https://doi.org/10.1109/TEC.2006.874229.

[57] L. Barzacchi, M. Lagnoni, R. Di Rienzo, A. Bertei, F. Baronti, Enabling early detection of lithium-ion battery degradation by linking electrochemical properties to equivalent circuit model parameters, J Energy Storage 50 (2022) 104213, https://doi.org/10.1016/j.est.2022.104213.

[58] C.H. Jeon, Y. Lee, R. Kim, S. Kim, D.K. Kim, Development of equivalent circuit model for thermal runaway in lithium-ion batteries, J Energy Storage 74 (2023) 109318, https://doi.org/10.1016/j.est.2023.109318.

[59] Dassoult Systemes, Dymola Software. https://www.3ds.com/it/prodotti-eservizi/catia/prodotti/dymola/ (n.d.).

[60] K. Makinejad, R. Arunachala, S. Arnold, H. Ennifar, H. Zhou, A. Jossen, W. Changyun, A lumped electro-thermal model for Li-ion cells in electric vehicle application, World Electric Vehicle Journal 7 (2015) 1–13, https://doi.org/10.3390/wevj7010001.

[61] M. Auch, T. Kuthada, S. Giese, A. Wagner, Influence of lithium-ion-battery equivalent circuit model parameter dependencies and architectures on the predicted heat generation in real-life drive cycles, Batteries 9 (2023), https://doi.org/10.3390/batteries9050274.

[62] N. Damay, C. Forgez, M.-P. Bichat, G. Friedrich, Thermal modeling of large prismatic LiFePO4/graphite battery, Coupled thermal and heat generation models for characterization and simulation, J Power Sources 283 (2015) 37–45, https://doi.org/10.1016/j.jpowsour.2015.02.091.

[63] Y. Bai, L. Li, Y. Li, G. Chen, H. Zhao, Z. Wang, C. Wu, H. Ma, X. Wang, H. Cui, J. Zhou, Reversible and irreversible heat generation of NCA/Si–C pouch cell during electrochemical energy-storage process, Journal of Energy, Chemistry 29 (2019) 95–102, https://doi.org/10.1016/j.jechem.2018.02.016.

[64] J.A. Newman, K.E. Thomas-Alyea, Electrochemical Systems, Wiley, 2004.

[65] J. Newman, K.E. Thomas, H. Hafezi, D.R. Wheeler, Modeling of lithium-ion batteries, J. Power Sources 119–121 (2003) 838–843, https://doi.org/10.1016/S0378-7753(03)00282-9.

[66] A. Jokar, B. Rajabloo, M. Désilets, M. Lacroix, Review of simplified pseudo-two-dimensional models of lithium-ion batteries, J. Power Sources 327 (2016) 44–55, https://doi.org/10.1016/j.jpowsour.2016.07.036.

[67] M. Lagnoni, C. Nicolella, A. Bertei, Comparison of electrolyte transport modelling in lithium-ion batteries: concentrated solution theory vs generalized Nernst-Planck model, J. Electrochem. Soc. 169 (2022) 020570, https://doi.org/10.1149/1945-7111/ac51f4.

[68] R. Yazami, Y. Reynier, Thermodynamics and crystal structure anomalies in lithium-intercalated graphite, J. Power Sources 153 (2006) 312–318, https://doi.org/10.1016/j.jpowsour.2005.05.087.

[69] T. Gao, Y. Han, D. Fraggedakis, S. Das, T. Zhou, C.N. Yeh, S. Xu, W.C. Chueh, J. Li, M.Z. Bazant, Interplay of lithium intercalation and plating on a single graphite particle, Joule 5 (2021) 393–414, https://doi.org/10.1016/j.joule.2020.12.020.

[70] D.A. Cogswell, M.Z. Bazant, Coherency strain and the kinetics of phase separation in LiFePO4 nanoparticles, ACS Nano 6 (2012) 2215–2225, https://doi.org/10.1021/nn204177u.

[71] H. Zhao, H.D. Deng, A.E. Cohen, J. Lim, Y. Li, D. Fraggedakis, B. Jiang, B. D. Storey, W.C. Chueh, R.D. Braatz, M.Z. Bazant, Learning heterogeneous reaction kinetics from X-ray videos pixel by pixel, Nature 621 (2023) 289–294, https://doi.org/10.1038/s41586-023-06393-x.

[72] R.B. Smith, M.Z. Bazant, Multiphase porous electrode theory, J. Electrochem. Soc. 164 (2017) E3291–E3310, https://doi.org/10.1149/2.0171711jes.

[73] T.R. Ferguson, M.Z. Bazant, Nonequilibrium thermodynamics of porous electrodes, J. Electrochem. Soc. 159 (2012) A1967–A1985, https://doi.org/10.1149/2.048212jes.

[74] W. Dreyer, C. Guhlke, R. Müller, Overcoming the shortcomings of the Nernst-Planck model, Phys. Chem. Chem. Phys. 15 (2013) 7075–7086, https://doi.org/10.1039/c3cp44390f.

[75] W. Dreyer, J. Jamnik, C. Guhlke, R. Huth, J. Moškon, M. Gaberšček, The thermodynamic origin of hysteresis in insertion batteries, Nat. Mater. 9 (2010) 448–453, https://doi.org/10.1038/nmat2730.

[76] R. Malik, D. Burch, M. Bazant, G. Ceder, Particle size dependence of the ionic diffusivity, Nano Lett. 10 (2010) 4123–4127, https://doi.org/10.1021/nl1023595.

[77] G. Richardson, I. Korotkin, R. Ranom, M. Castle, J.M. Foster, Generalised single particle models for high-rate operation of graded lithium-ion electrodes: systematic derivation and validation, Electrochim. Acta 339 (2020) 135862, https://doi.org/10.1016/j.electacta.2020.135862.

[78] M. Lagnoni, C. Nicolella, A. Bertei, Survey and sensitivity analysis of critical parameters in lithium-ion battery thermo-electrochemical modeling, Electrochim. Acta 394 (2021), https://doi.org/10.1016/j.electacta.2021.139098.

[79] A. Frank, J. Sturm, M. Steinhardt, A. Rheinfeld, A. Jossen, Impact of current collector design and cooling topology on fast charging of cylindrical lithium-ion batteries, ECS Advances 1 (2022) 40502, https://doi.org/10.1149/2754-2734/ac97e0.

[80] F. Ciucci, W. Lai, Derivation of micro/macro lithium battery models from homogenization, Transp. Porous Media 88 (2011) 249–270, https://doi.org/10.1007/s11242-011-9738-5.

[81] M.Z. Bazant, Theory of chemical kinetics and charge transfer based on nonequilibrium thermodynamics, Acc. Chem. Res. 46 (2013) 1144–1160, https://doi.org/10.1021/ar300145c.

[82] R.B. Smith, E. Khoo, M.Z. Bazant, Intercalation kinetics in multiphase-layered materials, J. Phys. Chem. C 121 (2017) 12505–12523, https://doi.org/10.1021/acs.jpcc.7b00185.

[83] A.A. Wang, S.E.J. O'Kane, F. Brosa Planella, J. Le Houx, K. O'Regan, M. Zyskin, J. Edge, C.W. Monroe, S.J. Cooper, D.A. Howey, E. Kendrick, J.M. Foster, Review of parameterisation and a novel database (LiionDB) for continuum Li-ion battery models, Progress, Energy 4 (2022), https://doi.org/10.1088/2516-1083/ac692c.

[84] P.M. Muñoz, R.M. Humana, T. Falagüerra, G. Correa, Parameter optimization of an electrochemical and thermal model for a lithium-ion commercial battery, J Energy Storage 32 (2020) 101803, https://doi.org/10.1016/j.est.2020.101803.

[85] A. Maheshwari, M.A. Dumitrescu, M. Destro, M. Santarelli, Inverse parameter determination in the development of an optimized lithium iron phosphate – graphite battery discharge model, J. Power Sources 307 (2016) 160–172, https://doi.org/10.1016/j.jpowsour.2015.12.111.

[86] A. Maheshwari, M.A. Dumitrescu, M. Destro, M. Santarelli, A modelling approach to understand charge discharge differences in thermal behaviour in lithium iron phosphate – graphite battery, Electrochim. Acta 243 (2017) 129–141, https://doi.org/10.1016/j.electacta.2017.05.049.

[87] P.P. Prosini, M. Lisi, D. Zane, M. Pasquali, Determination of the chemical diffusion coefficient of lithium in LiFePO4, Solid State Ionics 148 (2002) 45–51, https://doi.org/10.1016/S0167-2738(02)00134-0.

[88] L.H. Saw, Y. Ye, A.A.O. Tay, Electrochemical–thermal analysis of 18650 lithium iron phosphate cell, Energy Convers. Manag. 75 (2013) 162–174, https://doi.org/10.1016/j.enconman.2013.05.040.

[89] I.V. Thorat, T. Joshi, K. Zaghib, J.N. Harb, D.R. Wheeler, Understanding rate-limiting mechanisms in LiFePO4 cathodes for Li-ion batteries, J. Electrochem. Soc. 158 (2011) A1185, https://doi.org/10.1149/2.001111jes.

[90] M. Mastali, E. Foreman, A. Modjtahedi, E. Samadani, A. Amirfazli, S. Farhad, R. A. Fraser, M. Fowler, Electrochemical-thermal modeling and experimental validation of commercial graphite/LiFePO4 pouch lithium-ion batteries, Int. J. Therm. Sci. 129 (2018) 218–230, https://doi.org/10.1016/j.ijthermalsci.2018.03.004.

[91] M.C. Yagci, R. Behmann, V. Daubert, J.A. Braun, D. Velten, W.G. Bessler, Electrical and structural characterization of large-format lithium iron phosphate cells used in home-storage systems, Energ. Technol. 9 (2021) 2000911, https://doi.org/10.1002/ente.202000911.

[92] J. Chiew, C.S. Chin, W.D. Toh, Z. Gao, J. Jia, C.Z. Zhang, A pseudo three-dimensional electrochemical-thermal model of a cylindrical LiFePO4/graphite battery, Appl. Therm. Eng. 147 (2019) 450–463, https://doi.org/10.1016/j.applthermaleng.2018.10.108.

[93] T. Danner, M. Singh, S. Hein, J. Kaiser, H. Hahn, A. Latz, Thick electrodes for Li-ion batteries: a model based analysis, J. Power Sources 334 (2016) 191–201, https://doi.org/10.1016/j.jpowsour.2016.09.143.

[94] M. Verbrugge, D. Baker, B. Koch, X. Xiao, W. Gu, Thermodynamic model for substitutional materials: application to lithiated graphite, spinel manganese oxide, iron phosphate, and layered nickel-manganese-cobalt oxide, J. Electrochem. Soc. 164 (2017) E3243, https://doi.org/10.1149/2.0341708jes.

[95] L.O. Valoén, J.N. Reimers, Transport properties of LiPF[sub 6]-based Li-ion battery electrolytes, J. Electrochem. Soc. 152 (2005) A882, https://doi.org/10.1149/1.1872737.

[96] M. Ender, J. Joos, T. Carraro, E. Ivers-Tiffée, Three-dimensional reconstruction of a composite cathode for lithium-ion cells, Electrochem. Commun. 13 (2011) 166–168, https://doi.org/10.1016/j.elecom.2010.12.004.

[97] V. Srinivasan, J. Newman, Discharge model for the lithium iron-phosphate electrode, J. Electrochem. Soc. 151 (2004) A1517, https://doi.org/10.1149/1.1785012.

[98] N. Nadkarni, E. Rejovitsky, D. Fraggedakis, C.V. Di Leo, R.B. Smith, P. Bai, M. Z. Bazant, Interplay of phase boundary anisotropy and electro-auto-catalytic surface reactions on the lithium intercalation dynamics in LiXFePO4 plateletlike nanoparticles, Phys Rev Mater 2 (2018), https://doi.org/10.1103/PhysRevMaterials.2.085406.

[99] COMSOL AB, COMSOL Multiphysics® v. 6.1. www.comsol.com (Stockholm, Sweden, n.d.).

[100] J.L. Dodd, Phase composition and dynamical studies of lithium iron phosphate. https://api.semanticscholar.org/CorpusID:137029917, 2007.

[101] V.V. Viswanathan, D. Choi, D. Wang, W. Xu, S. Towne, R.E. Williford, J.-G. Zhang, J. Liu, Z. Yang, Effect of entropy change of lithium intercalation in cathodes and anodes on Li-ion battery thermal management, J. Power Sources 195 (2010) 3720–3729, https://doi.org/10.1016/j.jpowsour.2009.11.103.

[102] J. Peng, J. Meng, J. Wu, Z. Deng, M. Lin, S. Mao, D.-I. Stroe, A comprehensive overview and comparison of parameter benchmark methods for lithium-ion battery application, J Energy Storage 71 (2023) 108197, https://doi.org/10.1016/j.est.2023.108197.

[103] M. Safari, C. Delacourt, Modeling of a commercial graphite/LiFePO4 cell, J. Electrochem. Soc. 158 (2011) A562, https://doi.org/10.1149/1.3567007.

Abbreviations

BMS: Battery management system
CC: Constant current operation
CV: Constant voltage operation
CCCV: Constant current constant voltage operation
ECM: Equivalent circuit model
LIB: Li-ion battery
MST: Multiple step test
OCV: Open circuit voltage
P2D: Pseudo-2-dimensional approach
PBM: Physics-based model
SOC: State of charge
SOH: State of health
WLTC: Worldwide harmonised light vehicles test cycle

Nomenclature

A_{act}: Cross sectional area of the electrodes [m^2]
A_{am}: Active material surface per unit of electrode volume [m^{-1}]
A_{ext}: Battery external surface affected by cooling [m^2]
a: Characteristic interface length [m]
C_{nom}: Nominal capacity of the battery [Ah]
C_{rated}: Rated capacity of the battery at C/3 [Ah]
C_n: Capacitance of the ECM ($n = 1, 2$) [F]
c: Li ions concentration in the electrolyte [$\mathrm{mol\ m}^{-3}$]
c^{in}: Initial Li concentration in the electrolyte [$\mathrm{mol\ m}^{-3}$]
c_p: Equivalent specific heat of the battery [$\mathrm{J\ kg}^{-1}\ \mathrm{K}^{-1}$]
$\widetilde{c}_s$: State of lithiation [–]
c_s^{max}: Maximum molar concentration of intercalated Li in the active material [$\mathrm{mol\ m}^{-3}$]
$\widetilde{c}_s^{min/max}$: Maximum and minimum state of lithiation [–]
$\widetilde{D}$: Ambipolar diffusivity of the electrolyte [$\mathrm{m}^2\ \mathrm{s}^{-1}$]
D_s: Chemical diffusion coefficient of intercalated Li in LFP [$\mathrm{m}^2\ \mathrm{s}^{-1}$]
$\overline{D}_s$: Intrinsic diffusion coefficient of intercalated Li in graphite [$\mathrm{m}^2\ \mathrm{s}^{-1}$]
D_s°: Chemical diffusion coefficient of intercalated Li in LFP at 25 °C [$\mathrm{m}^2\ \mathrm{s}^{-1}$]
$\overline{D}_s^{\circ}$: Intrinsic diffusion coefficient of intercalated Li in graphite at 25 °C [$\mathrm{m}^2\ \mathrm{s}^{-1}$]
E°: Standard equilibrium potential of graphite [V]
E_{D_s}: Activation energy for diffusion coefficient [$\mathrm{J\ mol}^{-1}$]
$E_{k_{ct}}$: Activation energy for charge transfer kinetic constant [$\mathrm{J\ mol}^{-1}$]
EHC: Entropic heat coefficient [$\mathrm{V\ K}^{-1}$]
F: Faraday constant [$\mathrm{C\ mol}^{-1}$]

h: Convective heat transfer coefficient [W m^{-2} K^{-1}]
i_{cell}: Applied current [A]
i_n: Current through the resistor $\mathrm{R_n}$ ($n = 1, 2$) [A]
J_{conc}: Li ion flux in the electrolyte as areal current density [A m^{-2}]
J_{ct}: Areal charge-transfer current density [A m^{-2}]
J_{ct}^{V}: Volumetric charge-transfer current density [A m^{-3}]
J_1: Total areal current density of electron-conducting phase [A m^{-2}]
J_2: Total current density in the electrolyte phase [A m^{-2}]
k_{ct}: Charge-transfer kinetic constant [A m$^{5/2}$ mol$^{-3/2}$]
k_{ct}°: Charge-transfer kinetic constant at 25 °C [A m$^{5/2}$ mol$^{-3/2}$]
L: Thickness of the domain [m]
M: Mass of the battery [kg]
N_{cell}: Number of battery unit cells [–]
N_s: Intercalated Li molar flux [mol m^{-2} s^{-1}]
$\dot{Q}_{ohm}$: Ohmic heat generation per unit of component volume [W m^{-3}]
$\dot{Q}_{rev}$: Reversible heat generation per unit of component volume [W m^{-3}]
$\dot{Q}_{rxn}$: Reaction heat generation per unit of component volume [W m^{-3}]
q_{ex}: Heat removed by convection in the thermal-ECM [W]
q_{gen}: Ideal power generator for the thermal-ECM [W]
q_{irr}: Irreversible power generation for the thermal-ECM [W]
q_{rev}: Reversible power generation for the thermal-ECM [W]
$\dot{q}_i$: Total heat generation of single component per unit cell volume ($i = N, S, P$) [W m^{-3}]
$\dot{q}_V$: Total heat generation per unit active volume [W m^{-3}]
R: Universal gas constant [J mol^{-1} K^{-1}]
R_{conv}: Convective thermal resistance used for the thermal-ECM [K W^{-1}]
R_n: Resistor of the ECM ($n = 1, 2$) [Ω]
r: Average particle radius of the active material [m]
T: Temperature of the cell [K]
T_{amb}: Ambient temperature of the climatic chamber [K]
T_{ref}: Reference temperature [K]
t_+: Transference number of Li ions [–]
U_{eq}: Equilibrium potential of the active material [V]
V_{act}: Active volume of the battery [m^3]
V_{CV}: Voltage value for constant voltage operation [V]
V_{oc}: Open circuit voltage of the cell of the equivalent circuit model [V]
$V_{oc,ref}$: Open circuit voltage of the cell of the equivalent circuit model at 25 °C [V]
v: Voltage of the cell for the ECM [V]

Greek

α: Symmetry coefficient of Butler-Volmer equation [–]
β: Bruggeman coefficient [–]
$\gamma_{\pm}$: Thermodynamic factor of the electrolyte [–]
ε: Volume fraction [–]
η_{act}: Activation overpotential of intercalation reaction [V]
$\tilde{\mu}_e^*$: Reduced electrochemical potential of electrons [V]
$\tilde{\mu}_+^*$: Reduced electrochemical potential of Li ions [V]
μ: Chemical potential of Li in graphite [J mol^{-1}]
μ_{eq}: Equilibrium chemical potential of Li in graphite at 25 °C [J mol^{-1}]
σ: Ionic conductivity of the electrolyte [S m^{-1}]
$\sigma_{e,eff}$: Effective electrical conductivity of electron-conducting phase [S m^{-1}]
τ: Tortuosity factor [–]
τ_n: RC time constant [s]

Subscripts

0: Pure ohmic resistor of the ECM
1: Component of the ECM first RC circuit
2: Component of the ECM second RC circuit
CC: Current collector phase
el: Electro-conductive phase
ey: Electrolyte phase
fill: Filler phase
N: Negative electrode
P: Positive electrode
ref: Quantity evaluated at $T = 25$ °C
S: Separator
s: Active material phase